

STATISTICAL MODELING OF EARTH'S PLASMAPAUSE

by

Victoir Veibell  
A Dissertation  
Submitted to the  
Graduate Faculty  
of  
George Mason University  
In Partial fulfillment of  
The Requirements for the Degree  
of  
Doctor of Philosophy  
Computational Space Sciences and Astrophysics

Committee:

\_\_\_\_\_  
Robert Weigel, Dissertation Director

\_\_\_\_\_  
Kirk Borne, Committee Member

\_\_\_\_\_  
Fernando Camelli, Committee Member

\_\_\_\_\_  
Jie Zhang, Committee Member

\_\_\_\_\_  
Maria Dworzecka, Department Chair

\_\_\_\_\_  
Peggy Agouris, Dean, The College of Science

Date: \_\_\_\_\_  
Spring Semester 2016  
George Mason University  
Fairfax, VA

Statistical Modelling of Earth's plasmasphere

A dissertation submitted in partial fulfillment of the requirements for the degree of  
Doctor of Philosophy at George Mason University

By

Victoir Veibell  
Master of Science  
George Mason University, 2014  
Bachelor of Science  
Embry Riddle Aeronautical University, 2010

Director: Robert Weigel, Professor  
Department of Physics and Astronomy

Spring Semester 2016  
George Mason University  
Fairfax, VA

Copyright © 2016 by Victoir Veibell  
All Rights Reserved

## **Dedication**

I dedicate this dissertation to ... I dedicate this dissertation to ...

## **Acknowledgments**

I would like to thank the following people who made this possible ... I would like to thank the following people who made this possible ...

## Table of Contents

	Page
List of Tables . . . . .	vii
List of Figures . . . . .	viii
Abstract . . . . .	0
1 Introduction . . . . .	1
1.1 Background . . . . .	1
1.1.1 Magnetosphere . . . . .	1
1.1.2 Radiation Belts . . . . .	6
1.1.3 Plasmasphere . . . . .	9
1.1.4 Statistical Modeling of Magnetosphere and Plasmasphere . . . . .	12
2 Models . . . . .	16
2.1 Linear . . . . .	16
2.1.1 Overview . . . . .	16
2.1.2 ARX . . . . .	16
2.1.3 ARMAX . . . . .	19
2.1.4 Applicability . . . . .	20
2.1.5 Caveats and Biases . . . . .	20
2.1.6 Summary . . . . .	23
2.2 Nonlinear . . . . .	23
2.2.1 Overview . . . . .	23
2.2.2 Neural Networks . . . . .	24
2.2.3 Applicability . . . . .	24
2.2.4 Caveats and Biases . . . . .	24
2.2.5 Comparison to Linear Model . . . . .	25
2.2.6 Summary . . . . .	26
3 Measurements . . . . .	27
3.1 Solar Wind . . . . .	27
3.1.1 Source . . . . .	29
3.1.2 Coverage . . . . .	29
3.1.3 Data preparation . . . . .	29

3.2	Geomagnetic . . . . .	30
3.2.1	Source . . . . .	30
3.2.2	Coverage . . . . .	30
3.2.3	Data preparation . . . . .	30
3.3	Plasmasphere . . . . .	31
3.3.1	Source . . . . .	32
3.3.2	Coverage . . . . .	32
3.3.3	Data preparation . . . . .	32
4	Analysis . . . . .	33
4.1	Overview . . . . .	33
4.2	Linear Correlations . . . . .	33
4.3	Nonlinear Correlations . . . . .	35
4.4	$F_{10.7}$ Dependence . . . . .	36
4.5	$B_z$ Dependence . . . . .	40
5	Onset Classification . . . . .	44
5.1	Method . . . . .	44
5.2	Results . . . . .	44
A	An Appendix . . . . .	47
	Bibliography . . . . .	48

## List of Tables

Table	Page
4.1 Table of linear model correlations showing the median of 100 random samples. Each sample trained on half of the data (via randomly selected rows of the least squares matrix) and tested on the other half . . . . .	35
4.2 Table of differences in linear training-testing models, where each correlation is the median correlation of 100 random samples. Each sample trained on half of the data (via randomly selected rows of the least squares matrix) and tested on the other half . . . . .	35
4.3 Table of nonlinear model test correlations showing the median of 100 random samples. Each sample trained on half of the data (via randomly selected rows of the least squares matrix) and tested on the other half . . . . .	36
4.4 Table of differences in nonlinear training-testing models, where each correlation is the median correlation of 100 random samples. Each sample trained on half of the data (via randomly selected rows of the least squares matrix) and tested on the other half . . . . .	36

## List of Figures

Figure	Page
1.1 Overview of inner magnetosphere <b>Make less ugly. From <a href="https://www.nasa.gov/mission_pages/mag-mos.html">https://www.nasa.gov/mission_pages/mag-mos.html</a></b> . . . . .	2
1.2 Currents in/around the magnetosphere [Stern, 1994] . . . . .	3
1.3 Top-down schematic of particle drift [Gold, 1959] . . . . .	4
1.4 Data from GOES 6 around March 1989 geomagnetic storm . . . . .	5
1.5 Motion of magnetically trapped particles [Walt, 1994] . . . . .	7
1.6 Relative position of plasmasphere (blue) and radiation belts (red) with varying geomagnetic activity levels [Carreau, 2013]. . . . .	8
1.7 Plasmapause position varying with $K_p$ [Lemaire, 1998] . . . . .	10
1.8 Plasmasphere dusk-side bulge with and without geomagnetic activity [Lemaire, 1998]. <b>What to do with existing caption?</b> . . . . .	11
2.1 (a) $D_{st}$ (black), persistence (red), 12-hour impulse response model (blue). (b) $v_{B_S}$ impulse as input. . . . .	17
2.2 Correlation between prediction and measurement vs lead time of forecast .	21
2.3 Nonlinear models (left) vs linear models (right) of $\rho_{eq}$ . . . . .	25
3.1 Data from GOES 6 with dashed lines indicating default storm thresholds .	28
3.2 Detection rate of $f_{T3.30m}$ for magnetic latitudes of 5, 9, and 11 degrees (curves A, B, and C respectively). From [Takahashi et al., 2010]. . . . .	31
4.1 Median $\rho_{eq}$ binned by local time, and availability of $\rho_{eq}$ with local time. .	34
4.2 Top: Comparing $F_{10.7.27d}$ and $\log(\rho_{eq.27d})$ using GOES 6 data. Bottom: Same as top, but all available satellites . . . . .	37
4.3 $F_{10.7}$ and $\log(\rho_{eq})$ correlation at varying time scales . . . . .	38
4.4 $\rho_{eq}$ and $D_{st}$ of events binned by median $F_{10.7}$ values. <b>Temerin and Li <math>D_{st}</math> model. Bz seems to have little impact.</b> . . . . .	39
4.5 $\rho_{eq}$ events binned by median $B_z$ before and after event onset . . . . .	41

4.6	$D_{st}$ predicted by nonlinear model of day of year. Bottom: Same, but including a dimension for $B_z$ . <b>See/improve DoYDst figure . . . . .</b>	43
5.1	Prediction confusion matrix for hourly (left) and daily (right) $\rho_{eq}$ onset events	45
5.2	Histogram of onset conditions for $\rho_{eq}$ events binned by correctness of prediction	45

## **Abstract**

STATISTICAL MODELLING OF EARTH'S PLASMASPHERE

Victoir Veibell, PhD

George Mason University, 2016

Dissertation Director: Robert Weigel

This dissertation intends to first: be a survey of current forecasting capabilities of statistical and magnetohydrodynamic (MHD) methods of Earth's magnetosphere, and second: attempt to improve upon forecasting methods by investigating the usefulness of various new models on both real and modeled data. The forecasting will be separated into two parts: that focusing on rare, but significant events (e.g. geomagnetic storms), and that focusing on general day-to-day predictions. It will encompass three main methods of forecasting: impulse response functions (IRF), nonlinear methods, and statistical methods that attempt to forecast MHD.

# Chapter 1: Introduction

## 1.1 Background

Add introductory paragraph that summarizes each section and how they're all connected, and how they're related to thesis work (e.g. Plasmasphere is where the data is focused, but greater magnetosphere is still talked about because coupling)

### 1.1.1 Magnetosphere

#### Discovery

The dynamic processes of Earth's magnetosphere and their various impacts on the planet and its inhabitants have been studied for centuries: from Celsius and Hiorter who noted a correlation between compass orientation and aurora [Soon and Yaskell, 2003] to the Carrington event in 1859 that established the connection between solar output and electromagnetic effects on Earth [Carrington, 1859].

It was not until Van Allen performed his rocket sounding and satellite measurements of high altitude cosmic rays, finding the eponymous Van Allen Radiation Belt, that the structure of the magnetosphere was generally accepted to be more complex than that of a basic dipole magnet [Newell, 2011]. Gold [1959] showed that charged particles captured from the solar wind plasma are broken into constituent parts that drift in opposing directions around the Earth, leading to a deeper understanding of the behavior the magnetosphere and its interconnectivity with structures both inwards and outwards, which in turn allowed for better forecasting of ground-based effects based on solar wind conditions.

The inner magnetosphere is composed of three main constituent parts: the plasmasphere, the ring current, and the radiation belts, all of which are shown in Figure 1.1.

**Find figure for entire magnetosphere, not just inner (maybe swap 1.2 and 1.1)**

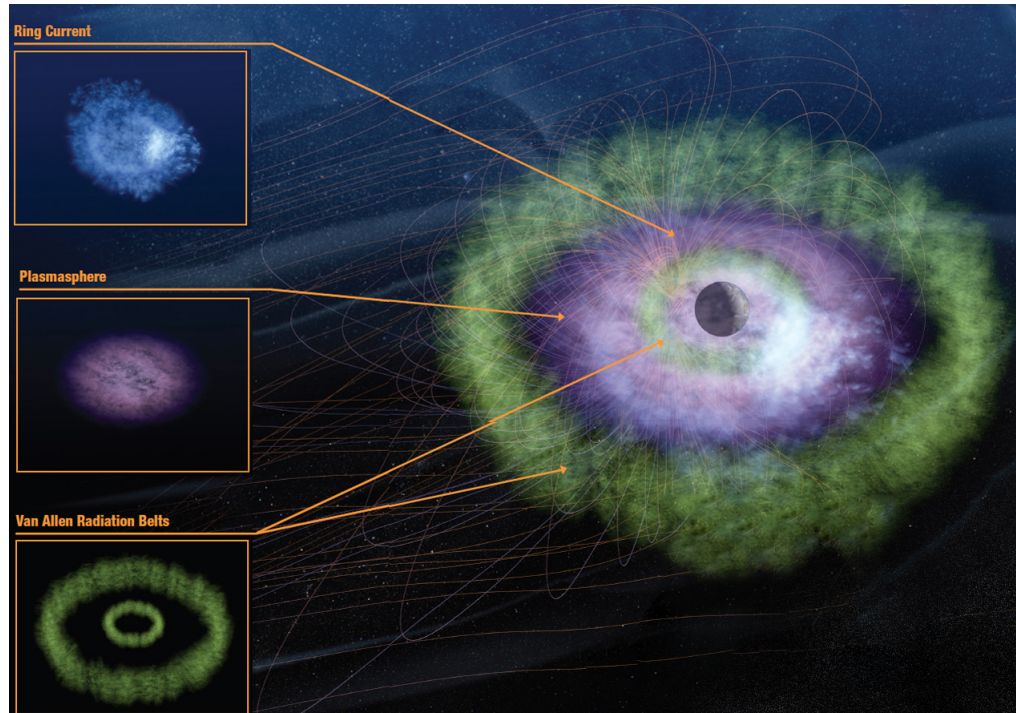


Figure 1.1: Overview of inner magnetosphere **Make less ugly.** From [https://www.nasa.gov/mission\\_pages/sunearth/science/inner-mag-mos.html](https://www.nasa.gov/mission_pages/sunearth/science/inner-mag-mos.html)

## Processes

The complex structure of the magnetosphere and plasmasphere leads to a number of distinct behaviors and processes such as ring currents, and geomagnetic storms and substorms, all of which are driven by the solar wind.

The Ring Current, one of the major magnetospheric currents shown in Figure 1.2, is composed of charged particles drifting opposite directions around the Earth based on their polarity. A schematic of this from a top-down perspective is shown in Figure 1.3.

With enough energetic particles drifting together, a current is generated that can significantly affect the magnetic field measured on Earth's surface. These particles in the current are energized into the magnetosphere via conditions that cause the solar wind's magnetic field to reconnect with that of Earth, which is often exacerbated by the surge of energy created by geomagnetic storms. **Storm time vs quiet time ring current**  
<http://onlinelibrary.wiley.com/doi/10.1002/2016GL068013/full> and **ring current/radiation belt** <http://www.leif.org/EOS/JZ066i005p01321.pdf>

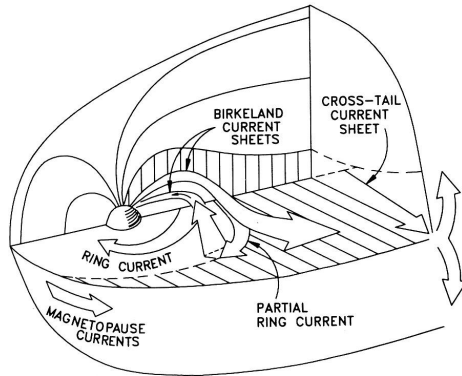


Figure 1.2: Currents in/around the magnetosphere [Stern, 1994]

Geomagnetic storms occur when the solar wind interacts with the Earth's magnetosphere in such a way as to produce significant disruptions in its normal, quiet-time, behavior. A geomagnetic storm is generally defined by a significant change to the magnetic field measured by multiple ground-based magnetometer measurements from stations spread around the world, in the case of the  $K_P$  index, or around the geomagnetic equator in the case of the disturbance storm-time ( $D_{st}$ ) index. These indices are used to classify storms into categories of severity [Oceanic and Administration, 2005]. The definition of storms in the literature varies slightly between authors [Yermolaev and Yermolaev, 2006], but most agree that sustained and abnormally perturbed near-earth and mid to low geomagnetic latitude magnetic field strengths over several hours or more constitutes a geomagnetic storm [Gosling et al., 1991].

Geomagnetic substorms, in contrast with storms, are much shorter; typically only lasting for an hour or two, and potentially happening soon after one another. They tend to have

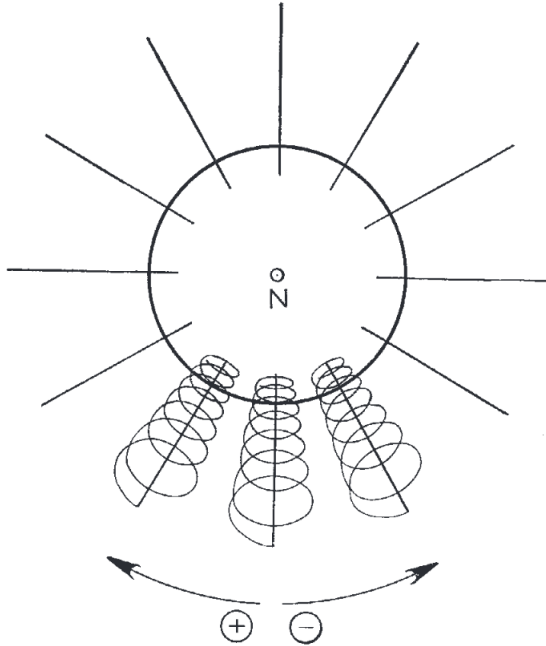


Fig. 2. Captive particle orbits, schematically, as seen from above the North Pole. Electrons will drift slowly eastwards, positive ions westwards

Figure 1.3: Top-down schematic of particle drift [Gold, 1959]

a less appreciable effect on the amount of particles/energy in the ring current, and are associated with sudden changes in energy coming from the tail of the magnetosphere rather than the dayside reconnections associated with storms [Gonzalez et al., 1994]. Figure 1.4 serves as an example of this, where a long, high-intensity storm is punctuated with a few small, short disturbances in both  $B_z$  and  $D_{st}$ .

Geomagnetic storms and substorms can have significant impacts on Earth and space systems, from inducing currents in large power grids to harming satellite circuitry and on-board data [Allen et al., 1989]. Because of the potential damage of such events, any ability to forecast a storm could allow operators to prevent or mitigate problems in their systems. Because of the large correlation of CMEs with geomagnetic storms [Yermolaev and Yermolaev, 2006], it can be estimated that our forewarning time is the difference between observing a CME (via visual or X-ray methods) and its propagation time plus magnetospheric interaction time. This time can span from one to five days, depending on the speed of the CME

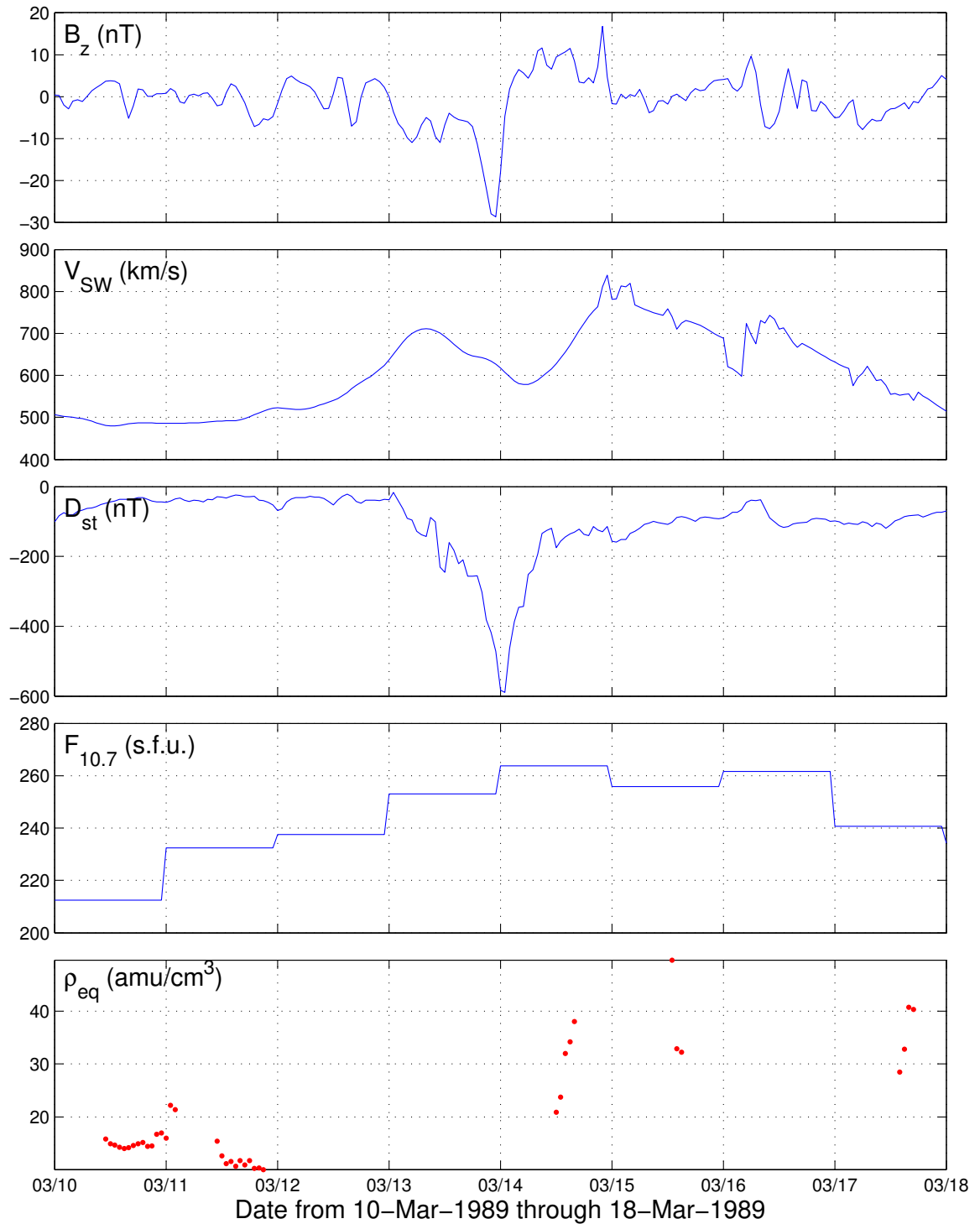


Figure 1.4: Data from GOES 6 around March 1989 geomagnetic storm

and how it interacts with the interplanetary medium [Zhang et al., 2007]. With a light speed delay of only eight minutes, this is ample time to see a storm approaching Earth and for operators to react, but a problem lies in the fact that storms are poorly predicted with such lead times [Weigel et al., 2006]. Some storms have slow onsets, some spike suddenly; some have high velocities, and some coincide with large amounts of high-energy particles; no single factor has yet proven to be a good predictor for storms, and while prediction has gradually improved over the years, there remains room for further study.

All of these processes are coupled to some degree with the plasmasphere, by transferring plasma and energy from the interplanetary medium to near Earth regions ( $\lesssim 8R_E$ ).

### 1.1.2 Radiation Belts

**Add more detail as to why radiation belts are discussed and how they're connected to the plasmasphere.**

#### Discovery

The radiation belts that surround Earth, known as the Van Allen Radiation Belts, are two (occasionally three [Darrouzet et al., 2013]) bands of energetic particles encircling the planet. The existence of such bands was theorized based on knowledge of magnetically trapped motion of charged particles; results from rocket soundings showed that more radiation exists in the auroral regions than at the equator. The beginning of the space age allowed particle counters to be launched onboard Explorer 1 and Explorer 3, which found radiation far beyond what was anticipated and concentrated into bands of high density [Newell, 2011].

#### Processes

The outer radiation belt is filled with electrons captured from the solar wind by the magnetosphere and then injected into the radiation belts from the magnetotail, and occasionally lost when the magnetopause moves back Earthward [cite](#). The inner belt tends to be filled

by heavier species from the ionosphere, and is overall less variable than the outer belt [Darnouzet et al., 2013]. The slot region between the two is formed by the interaction of energetic particles with very low frequency (VLF) waves, leading to particle loss to the atmosphere [Fung et al., 2006]. In contrast to the ring current particles, the radiation belt particles tend to have much higher energy

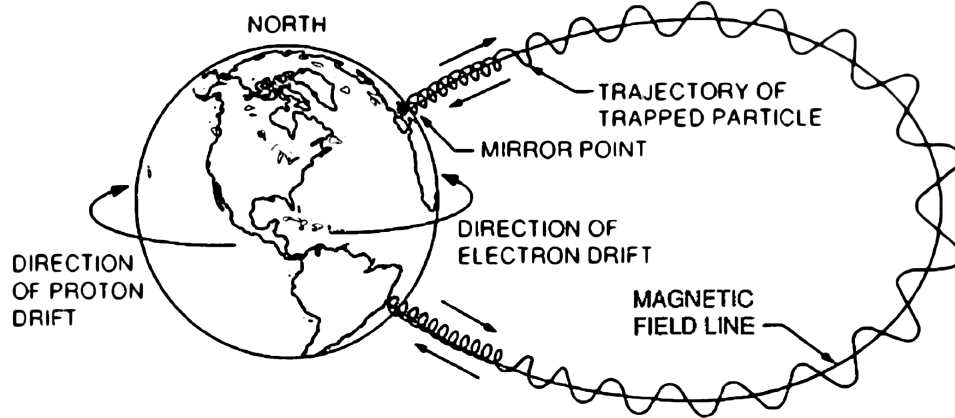


Figure 1.5: Motion of magnetically trapped particles [Walt, 1994]

The various forms of particle movement are shown in Figure 1.5. The primary component being the drift motion leading to the ring current. As particles approach the “Mirror point”, a slight angle between the motion and the curvature of the magnetic field line leads to a force opposing the motion along the line, eventually mirroring the particle back in the opposite direction. Because this applies to all particles within a certain range of energies and pitch angles, the collective sum of trapped particles forms the radiation belts. By modeling the particle mass, momentum, and the magnetic field strength of a given dipole magnetic field, approximations can be made regarding what amount of particles will become trapped in the field, and what amount will be lost to scattering [Young et al., 2008].

The radiation belts also have an impact on the plasmasphere by acting as an occasional source of low energy particles and a sink for high energy particles. The plasmasphere also acts on the radiation belts via the VLF waves, energizing electrons out of the plasmasphere and into the radiation belts, or providing particles already in the belts the energy needed to

become untrapped [Darrouzet et al., 2013]. While the outer limits of the plasmasphere and the outer radiation belt often coincide and react similarly to geomagnetic activity, they can become separated during geomagnetically active times [Darrouzet et al., 2013]. An example of this variation in relative position is shown in Figure 1.6.

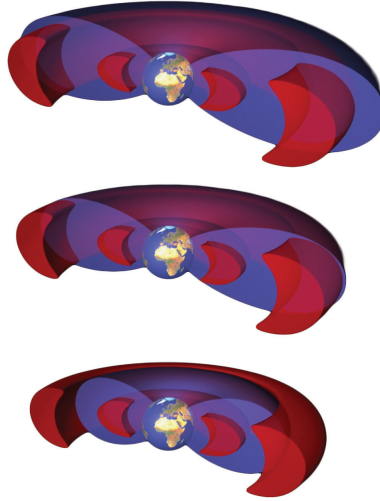


Figure 1.6: Relative position of plasmasphere (blue) and radiation belts (red) with varying geomagnetic activity levels [Carreau, 2013].

Another source/sink of energy for particles in the radiation belts (or general magnetospheric plasma) is via Alfvén waves [Keiling, 2009]. These waves are composed of oscillations of particles **Not particles? Verify** traveling along magnetic field lines, carrying both energy and field-aligned currents as they propagate. By moving energy along the field lines, Alfvén waves also couple the various distinct sections of plasma around Earth.

**denton paper for plasmasphere bounce motion [Young et al., 2008] and density along field line (cite?)**

### 1.1.3 Plasmasphere

#### Discovery

The plasmasphere, shown in Figure 1.1, was largely unknown until the beginning of the space age, being found both through analyses of very low frequency radio waves and in-situ spacecraft measurements. Previously, it was believed that electron density decreased continuously from the ionosphere to the interplanetary medium [Lemaire, 1998]. These experiments showed that the Earth had a sphere of cold plasma around it that ended in an abrupt boundary, and varied in location and density gradient with geomagnetic activity [Carpenter, 1966, Lemaire, 1998].

#### Processes

The plasmasphere is interconnected with the radiation belts and the ionosphere. While many of the specifics of this interaction are still not fully understood, some parts have been observed and explained to a reliable degree of accuracy.

In the ionosphere, during the daytime sunlight photoionizes oxygen which produces excess electrons that are transferred up via polar wind into the plasmasphere along magnetic field lines bringing energy and heat along with it. This daily “refilling” flux continues until a saturation point is reached, bringing the lower bounds of the plasmasphere into equilibrium with the upper ionosphere. This flux also typically reverses on the night side, sending electrons back down into the ionosphere [Lemaire, 1998].

During periods when the location of the plasmapause is quickly brought earthwards, or the plasmapause is re-established in a new location, plasma left outside the plasmapause is known to be magnetically convected outwards and sunwards [Carpenter and Lemaire, 1997, Lemaire, 1998], termed “eroding” the plasmasphere. This is because the location of the plasmapause can vary greatly with geomagnetic conditions. Figure 1.7 shows how the L-shell distance varies with magnetic activity via the  $K_p$  index.

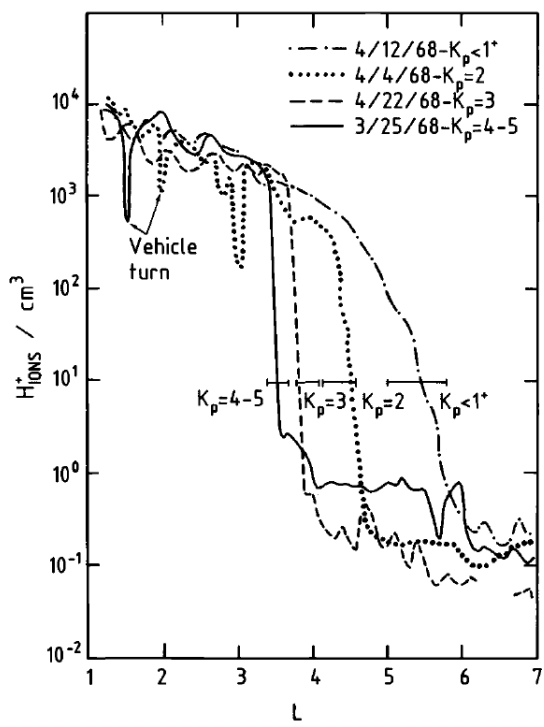


**Figure 3.5** A composite of several typical plasmapause crossings representing different levels of magnetic activity. These plots of hydrogen ion concentrations versus  $L$  represent outbound passes in the local time region from midnight to 0400 (after Chappell *et al.*, 1970a).

Figure 1.7: Plasmapause position varying with  $K_p$  [Lemaire, 1998]

Figure 1.7 also shows the plasmatrough; the low density region just outside the plasma-pause where particle count often drops multiple orders of magnitude from the plasmasphere and continues out through the magnetosphere.

At times, the plasmasphere becomes distorted at the plasmapause due to dayside reconnection, causing bulges that can become elongated and detached during co-rotation, usually on the dusk side. These extended segments of plasma are known as “plumes” and appear as a peak in density in a normally empty plasmatrough. These plumes also often occur with, and possibly because of, enhanced magnetospheric activity [Elphic et al., 1996]. This bulge, and the effects of geomagnetic activity on the bulge, is shown in Figure 1.8

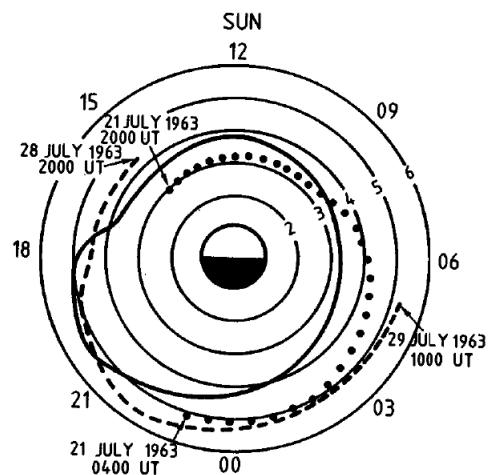


Figure 1.8: Plasmasphere dusk-side bulge with and without geomagnetic activity [Lemaire, 1998]. **What to do with existing caption?**

**Figure 2.10** Equatorial radius of the plasmapause. The solid line represents the average equatorial position of the knee versus local time, during periods of moderate, steady geomagnetic agitation ( $K_p = 2-4$ ). The observations were made in July and August, 1963 at Eights, Antarctica. The dots show a particular example involving increasing magnetic activity; the dashes illustrate an example of decreasing agitation (after Carpenter, 1966).

Need diagram for each paragraph in processes section

Leave off with list of things that are not well understood and how work in thesis approaches them.

#### 1.1.4 Statistical Modeling of Magnetosphere and Plasmasphere

Initial forecasts of geomagnetic disturbances were based on an observed time delay from sunspot sitings [Richardson, 1936]. The state of geomagnetic storm forecasting then advanced to a basic theory involving electromagnetic interactions in the magnetosphere [Chapman and Ferraro, 1931]. There now exist entire services dedicated to executing statistical and magnetohydrodynamic (MHD) based models of the magnetosphere [CCMC], as well as multi-year, multi-institution efforts to survey the general statistics of modeling and forecasting of extreme events [Ghil et al., 2011].

The convergence of the advancement in both statistical and MHD-based simulation has led to a situation where the scientific community has the capacity for monitoring and forecasting the near-Earth effects in real time. There have been efforts to test the forecast performance of select models over a small number of geomagnetic events [Bala and Reiff, 2012, Tsyganenko and Sitnov, 2005, Zhang et al., 2006, Yermolaev and Yermolaev, 2006] **Also CCMC papers (GEM challenge)**. However no research has been done that involves the analysis of long-term forecasting performance of these models and comparison of the results with existing methods.

Three main metrics of magnetospheric activity are seen throughout the literature; the  $K_p$  index: a measure of magnetosphere convection caused by currents induced by a changing plasma sheet (and indirectly from the global convection field strength) [Thomsen, 2004]; the  $AE$  index: a measure of electrojet activity based on the maximum and minimum field strength measurements from magnetometer stations at auroral latitudes [Davis and Sugiura, 1966]; and the previously mentioned  $D_{st}$  index based on magnetic field perturbations caused primarily by a changing ring current.

#### **Needs diagram showing how measurements are made**

Models specific to the plasmasphere and plasmatrough include Carpenter and Anderson's ISEE/Whistler Model of Equatorial Electron Density in the Magnetosphere, which use empirical data to determine the location and density of the saturated plasmasphere and

plasmatrough [Carpenter and Anderson, 1992]. Carpenter and Anderson [1992] analyze ISEE 1 data for drops in number density of at least a factor of 5 across half an L-shell and state that the inner edge of the plasmapause is located at  $L_{ppi} = 5.6 - 0.46K_{p_{max}}$ . Here  $K_{p_{max}}$  is the maximum value of  $K_p$  (an index averaging 11 mid-latitude stations in the previous 24 hours), and  $L$  is the set of magnetic field lines at a distance of  $L$  Earth radii at the magnetic equator. This specifies the outer boundary of the plasmasphere, and from there the density is modeled inwards as  $n_e = n_{eL_{ppi}} \cdot 10^{-(L-L_{ppi})/\Delta pp}$ , where  $n_{eL_{ppi}}$  relates day number, sunspot number, whistler profiles, and multiple year-long perturbations in an exponential fashion shown as  $n_e(L, d, \bar{R}) = 10^{\sum x_i}$ .  $L_{ppi}$  and  $\Delta pp$  are empirically derived plasmapause location and width, respectively.  $x_1$  is a whistler reference profile, and indices  $i = 2 - 4$  represent perturbation values for annual, semiannual, and solar cycle variations respectively. The exact numbers in the density profiles vary slightly between a midnight-06 MLT model, and a 06-15 MLT model, based on the specific passes used to fit the parameters for each section.

Gallagher et al. [2000] created a Global Core Plasma Model which combines empirically derived models of the ionosphere, plasmasphere, and magnetosphere. For the plasmasphere it links plasma density and magnetosphere conditions by fitting Carpenter's equation, but replacing their piecewise dependence on MLT with a sinusoidal term along with extra factors to account for the post-dusk bulge while still keeping the plasmasphere model continuous. At the most basic level, the plasmasphere component reduces to an exponential equation of the form  $n_{ps} = 10^{gh} - 1$ , where  $g$  and  $h$  are terms relating to the inner plasmasphere and plasmapause, combining sunspot number, day of year, and a plasmapause gradient term that accounts for the MLT dependence in the form of  $\Delta pp = 0.036 \cdot \sin(\frac{2\pi(MLT-6)}{24}) + 0.14$ . They also link plasmasphere filling time to  $K_p$ , stating it starts at 3.5 MLT and fills until a time of  $\Phi_{TP} = 0.145K_p^2 - 2.63K_p + 21.86$  hours Gallagher et al. [1995].

Moldwin et al. [2002] build on Carpenter's model by taking CRRES data and the same plasmapause detection parameters as Carpenter, finding 969 plasmapause detections

compared to the 40 used to derive the model in Carpenter and Anderson [1992]. Using the abundance of data they do statistical analyses such as showing a least squares linear fit between increasing  $K_p$  and decreasing L-shell of the plasmapause of the form  $L_{pp} = (5.39 \pm 0.072) - (0.382 \pm 0.019) \cdot K_p(max)$  with a correlation of 0.548. They also find that if they limit this to plasmapause crossings between 09 and 15 MLT, the linear correlation increases to 0.727.

O'Brien and Moldwin [2003] find that using auroral electrojet (AE) or disturbance storm time ( $D_{st}$ ) indices work better than  $K_p$  for determining plasmapause location. They use the same plasmapause crossings as Moldwin et al. [2002] and model them against hourly changes in the ring current (via  $D_{st}$ ) or 1-minute changes in the auroral electrojet currents (AE). They take the maximum (or minimum, as required) of each index over a varying range of hours, from a start of up to 72 hours before crossing up to end of at least 6 hours before crossing, and fit a basic linear model. Their three best models were a basic linear fit of  $L_{pp}$  to  $\max_{-36,-2} K_p$ ,  $\max_{-36,0} AE$ , and  $\log_{10}(\min_{-24,0} D_{st})$ . Using a bootstrap analysis for significance, all three models were indistinguishably similar in the root mean square error (RMSE) of their respective models, except for AE having significantly less error in the night sector than  $D_{st}$ . Making the model slightly more advanced by including a MLT dependence and periodic terms allows a bulge to be approximated, and finds that the allowing local time to be accounted for significantly (at the 95% confidence level) reduces the error of the model, but still shows no significant difference between models of the same complexity.

As for models specifically of the plasmatrough, Loto'aniu et al. [1999] take ground based Ultra Low Frequency (ULF) wave measurements, then map them to plasma mass densities between  $L = 4.5$  and  $L = 10$  via the Tsyganenko T89 magnetic field model and an  $R^{-4}$  plasma mass density profile. These estimated values were then compared to in-situ measurements from the CRRES satellite and found that this technique can, under specific conditions where all of the field lines at the ground stations map to plasmatrough, accurately measure plasmatrough mass density.

Takahashi et al. [2006] take a similar approach, but approximate ULF waves from the

CRRES satellite directly, instead of using ground stations, and then map that to mass density values. By using the electric field spectra on the satellite and finding a fundamental frequency of the toroidal waves, they estimate mass density with a combination of theoretical model and empirical observations. The magnetic field model used is either T89 or T96, dependent on  $K_p$  or  $D_{st}$  respectively. Instead of an  $R^{-4}$  dependence for the mass density model, they use  $\rho = \rho_{eq}(LR_E/R)^{0.5}$ , and then combine with frequency observations via  $\rho_{eq\_est} = \rho_{eq\_theory}(f_{1\_theory}/f_{1\_obs})^2$ .

Most of these studies focus on plasma density in the plasmapause and plasmasphere, since that is where the densities are the highest, easiest to measure, and have the most data availability. This study focuses on the plasmatrough partly due to it's unexplored nature, and largely due to the significance of the region to objects in geostationary orbits. It also couples with both the magnetosphere and plasmasphere, suggesting that a greater understanding of the behavior of the plasmatrough may aid in understanding the coupling of both major bordering regions.

**Takahashi (2010), Kondrashov 2014, Denton (2006, 2015), Min 2013, Tsy-ganenko models**

**Make connection to each paper with a section in chapter 2.**

## Chapter 2: Methods

This work utilized both linear and nonlinear methods for analysis, modeling, and prediction, including Auto-Regressive Moving Average models with eXogenous inputs (ARMAX) and neural net models. No single method is ideal, and using many methods is better for insight, especially for nonlinear/complex systems. The details of their application will be expanded upon in their respective sections.

### 2.1 Linear

#### 2.1.1 Overview

Due to its simplicity and ease of application, linear models are used in practically all fields as a first attempt to interpret data and any potential relationships. In Space Physics, where the underlying behavior of a complex system is not theoretically known, and in-situ measurements are sparse, linear models are often the first step towards understanding what components are related and to what degree. Sometimes this leads to understanding unexpected complexities in a system. **Example. Lemaire p.183 heavier ions in outer plasmasphere than inner plasmasphere? Correlation between plasmapause and radiation belt boundary?**

#### 2.1.2 ARX

Impulse response systems are systems in which the output (a response) is driven by a linear sum of coefficients of an input (a series of impulses). A simple example would be making a loud noise in a concert hall. The response will be the unique echoes and reverberations

created by the initial driving sound, and with enough signal, a statistical model can be generated that will map the input sound to a response echo. In the magnetosphere, the most used example is an impulse of  $v_{BS}$  driving the Auroral Electrojet (AE/AL) index [Bargatze et al., 1985], or the Disturbance Storm Time ( $D_{st}$ ) index [Clauer et al., 1981].  $v_{BS}$  is a metric where solar wind velocity is multiplied by the southward component of the solar wind magnetic field (i.e. southward components keep their value, northward components are zeroed). This model is shown in Figure 2.1

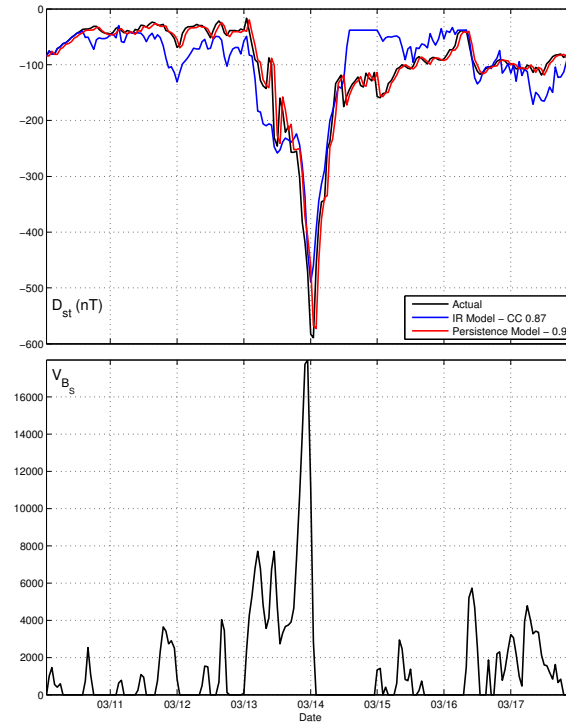


Figure 2.1: (a)  $D_{st}$  (black), persistence (red), 12-hour impulse response model (blue). (b)  $v_{BS}$  impulse as input.

This plot shows how different models are used to predict magnetospheric variables with varying amounts of success. In this proposal, what starts as a Box-Jenkins model of the form [Weigel, 2007]:

$$x(t) = \sum_{j=1}^m b_j \cdot f(t - j\Delta t) + c_t$$

can be modified to include an auto-regressive component to be an autoregressive model with exogenous inputs (ARX) such as that used in Klimas et al. [1998], taking the form:

$$\hat{x}(t) = \sum_{i=1}^l a_i \cdot x(t - i\Delta t) + \sum_{j=1}^m b_j \cdot f(t - j\Delta t) + c_t \quad (2.1)$$

Where  $m$  and  $l$  are the number of coefficients desired for including previous data points in the prediction, and  $c$  is a factor to remove the mean offset from the data. Note that in some cases the starting value of the iterators can be individually increased if there is a known delay in response time or there is a desire to predict further into the future. In Klimas et al. [1998], second order equations ( $m = 2$ ) were used with anywhere from one to four driving coefficients, but in practice any number of coefficients and any number of driving variables can be used up to some fraction of the number of data points that allows the coefficient matrices to be solved for.

There generally is a limit to the usefulness of large-lead-time forecasts Ghil et al. [2011]. By looking at a plot of the cross correlation relative to the number of coefficients, a limit will generally be seen where adding more coefficients no longer reduces error in the model. By creating a threshold of change in fit per coefficient added (perhaps via a bootstrap method), the minimum number of coefficients needed to optimally model the system can be determined.

By constructing a linear system of equations from Equation 2.1, the coefficients can be

solved for in a general matrix form (where, in this case,  $l = m$ ):

$$\begin{pmatrix} x_0 & \dots & x_{l-1} & f_0 & \dots & f_{l-1} & 1 \\ x_1 & & x_l & f_l & & f_l & 1 \\ \dots & & & & & & \\ x_{N-l} & \dots & x_{N-1} & f_{N-l} & \dots & f_{N-1} & 1 \end{pmatrix} \begin{pmatrix} a_0 \\ \dots \\ a_{l-1} \\ b_0 \\ \dots \\ b_{l-1} \\ c \end{pmatrix} = \begin{pmatrix} x_l \\ x_{l+1} \\ \dots \\ x_N \end{pmatrix}$$

This is a linear model for the behavior of a system. However, it has been shown that the set of coefficients describing the response of a system can change with storm intensity Klimas et al. [1998], the time scale modeled Vassiliadis et al. [2004], and even the time of day Bargatze et al. [1985]. This creates a very large number of possible directions for research, from predicting storm onsets, to predicting storm intensities, to modeling the overall shape and behavior of a storm, as well as all of the other possible interactions outside of storm-time.

### 2.1.3 ARMAX

A class of model known as an Auto-Regressive Moving Average with eXogenous inputs model (ARMAX) is often used in time series analysis to combine the effects of persistence, linear dependence, and an average that changes with time. It makes a slight change on the ARX model in Equation 2.1, adding the moving average term:

$$\hat{x}(t) = \sum_{i=1}^l a_i \cdot x(t - i\Delta t) + \sum_{j=1}^m b_j \cdot f(t - j\Delta t) + \sum_{k=1}^n e_j \cdot c(t - k\Delta t) + c_t \quad (2.2)$$

### 2.1.4 Applicability

As implied by the name, an ARMAX model is suitable for analysis of a time-dependent linear system where the value of a measurement is determined by its own persistence, an external variable, and some factor that contributes to a moving average with time. Most linear systems can be encapsulated by this framework, some even being overspecified with this level of accounting for variability.

### 2.1.5 Caveats and Biases

There will be a number of things that, ideally, must come together to make this kind of data prediction work. For one: ARX methods can often be heavily dependent on a concept known as “persistence”, whereby the best prediction for a variable at any time is that same variable at the last measured time step. For example, if the high temperature today is 70°, it is fairly likely that the high temperature tomorrow will be near 70°. Too much reliance on persistence forecasting, though, and predictions can lose their usefulness. Figure 2.1, for example, shows how a model can achieve high correlation with persistence, but be almost entirely useless for predicting events before they happen since the spikes are never anticipated, just modeled after they’ve already been seen. Also, if the time of interest is multiple time-steps ahead, a simple persistence forecast becomes less and less accurate with each step.

In this case, it is clear that the most recent measurement has the most weight in a forecast. For day-to-day behavior, this is acceptable as being part of the behavior of the system. For the forecasting of extreme events, however, another metric must be used that measures the ability of the model to predict events at or before their actual occurrence, while simultaneously avoiding predicting events that do not happen. One method for comparing models in this fashion is by using the Heidke Skill Score Heidke [1926], Brier and Allen [1951], which is based on the quantity:

$$S = \frac{R - E}{T - E}$$

**Drop this part if not actually used**

where  $R$  is the number of correct forecasts,  $T$  is the total number of forecasts, and  $E$  is the number expected to be correct by, in this case, a persistence forecast. This can be adapted to either consider a range of "correctness", or a binary threshold to be met. It may also be desired to assign a cost-weighting to success rates. If, say, it costs \$1 million to prepare a power grid for a storm, 10 false alarms to every one storm gets costly unless successfully preparing for that one storm saves \$1 billion. To do this, a measure of the utility of a forecast can be quantified Weigel et al. [2006]:

$$U_F \equiv BN_H - CN_{\bar{H}} > 0$$

Where  $N_H$  is the number of correct forecasts,  $N_{\bar{H}}$  is the number of false alarms,  $C$  is the cost of taking mitigating action, and  $B$  is the benefit from correctly taking mitigating action. This method has caveats discussed in Weigel et al. [2006], but is a useful metric for forecast utility when costs are known, and some measure of success can be determined.

The other major problem in forecasting is that of lead time. Being able to forecast a storm one minute in advance is generally not enough time for operators to take mitigating action.

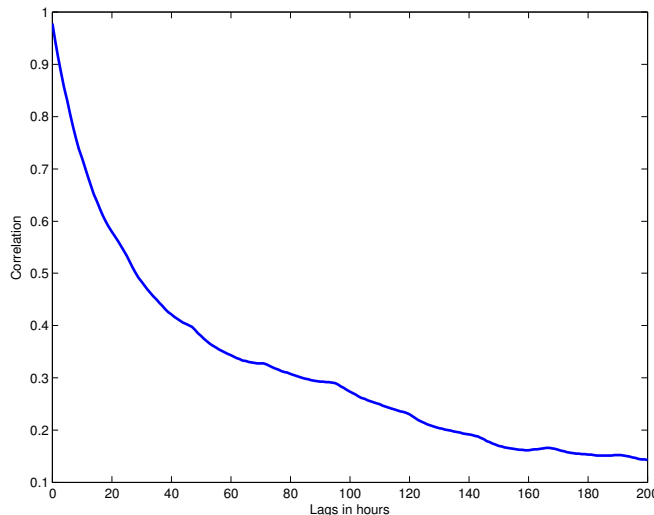


Figure 2.2: Correlation between prediction and measurement vs lead time of forecast

Figure 2.2 shows the correlation of a set of predictions made for autocorrelation in the disturbance storm time index ( $D_{st}$ ) against the amount of lead time in the forecasts. This metric is a measure of how much disturbances in the magnetosphere induce currents in ground-based electrical systems. The predictions were made further and further in time from the current magnetic field and  $D_{st}$  measurements, with decreasing accuracy as the predicted time got further from the current time. While an accurate prediction can be made one hour in advance, a prediction 3 days in advance has almost no correlation with what was measured. This is one of the main problems that this dissertation hopes to address.

### Mean vs Median

The question of whether to use means or medians for analysis is based on what facets of the data are most important to the research. Since means are biased towards outliers and medians biased against them [cite](#), the decision rests on how much weight should be given to outliers (or extreme values) in a study. For example, when looking at long-term solar wind variables, intermittent spikes may not be relevant to the overall pattern of behavior being analyzed, but knowing that on a short time scale a certain day had a noticeable spike may be important. In the former case, using the median would likely be best, and using the mean for the latter. However, space physics often deals with skewed distributions and sparse data, leading to an uncertainty of which method is best, so both are analyzed with their respective traits in mind. [Numerically specific result. E.g. 27 day F10.7 vs  \$\rho\_{eq}\$  with medians vs means](#)

### Effects of time averaging

Similarly to the mean vs median question, the decision on if/how much to average the data over time will affect the resulting time series to be biased against intermittent spikes in value. The more time added to any particular average, the less impact any short-term

changes will have on the final value.

### 2.1.6 Summary

Because linear models are simple, optimizable, and adequately model many physical systems, they are a useful first choice for trying to determine the behavior of mass density in the plasmatrough. The relationships between solar wind, plasmatrough, and plasmasphere may also be detectable on the first order approximation by a linear model if not entirely linear in nature.

## 2.2 Nonlinear

### 2.2.1 Overview

While many nonlinear systems are approximated by a number of localized linear models for the sake of simplicity and ease of interpretation, the design and implementation of nonlinear models has become greatly simplified in recent years. Their use allows for determining nonlinear structure without pre-assuming any localization of the data, and as such were used to attempt forecasting in this dissertation. The first choice was a model based on neural networks [Hernandez et al., 1993, Bala and Reiff, 2012] which approximates a non-linear system given a set of training data. The usefulness of this is apparent in a few key points: the weights of contribution of any particular variable to a system will likely be nonlinear in some fashion (e.g. a ground station's measurements will depend on sunlight heating the ionosphere which depends on latitude, time of year, and time of day), and allowing for the non-linear effects of saturation where perhaps the magnetosphere will behave differently after reaching certain levels of particle density or electric potential, rather than directly scaling regardless of limits.

Another algorithm known as Principal Component Analysis (PCA) can be used to take the large number of possible variables and define an orthogonal set of vectors that most efficiently encapsulate the variance in the data. By doing this, the number of variables

needed for computing any linear or non-linear algorithm can be reduced and optimized, making predictions quicker while maintaining most of the predictive benefits of using all possible data, as well as indicating which variables contain the most information relevant to the predictions.

### 2.2.2 Neural Networks

### 2.2.3 Applicability

Nonlinear models are applicable when a system has more complexity than can be encapsulated by a linear model. Since they're usually a class of model that trains adaptive weights that can be tuned by known inputs and outputs, they're especially useful for systems where a large amount of training data are available.

### 2.2.4 Caveats and Biases

Nonlinear models can be susceptible to overfitting, since they inherently attempt to fit more complexity than a linear model, but can also be controlled via the number of inputs and weights used. They also may suggest more structure than might truly exist. Both of these problems are lessened by training with more data, if available. Figure 2.3 shows a comparison of predicting equatorial mass density ( $\rho_{eq}$ ) with the  $F_{10.7}$  index and the disturbance storm time index ( $D_{st}$ ). The neural net models (left) shows much more structure than the linear models (right) despite being given the same data. Whether that structure reflects any real physical phenomenon, however, is a difficult problem to answer, and so both models are often compared to attempt to ascertain what structure may be valid.

Sometimes, as in the top two plots of Figure 2.3, the structure seems to support the same conclusion where the nonlinear model just adds slight detail. Othertimes, as in the case of the lower two plots, the results seem discrepant. The linear model indicates increasing  $\rho_{eq}$  with increasing  $B_z$  and increasing  $F_{10.7}$ , while the nonlinear model shows a more nuanced structure with increased  $\rho_{eq}$  showing up with lower  $B_z$  values, and at a range of  $F_{10.7}$  values. Situations like these require further analysis to determine the true underlying structure.

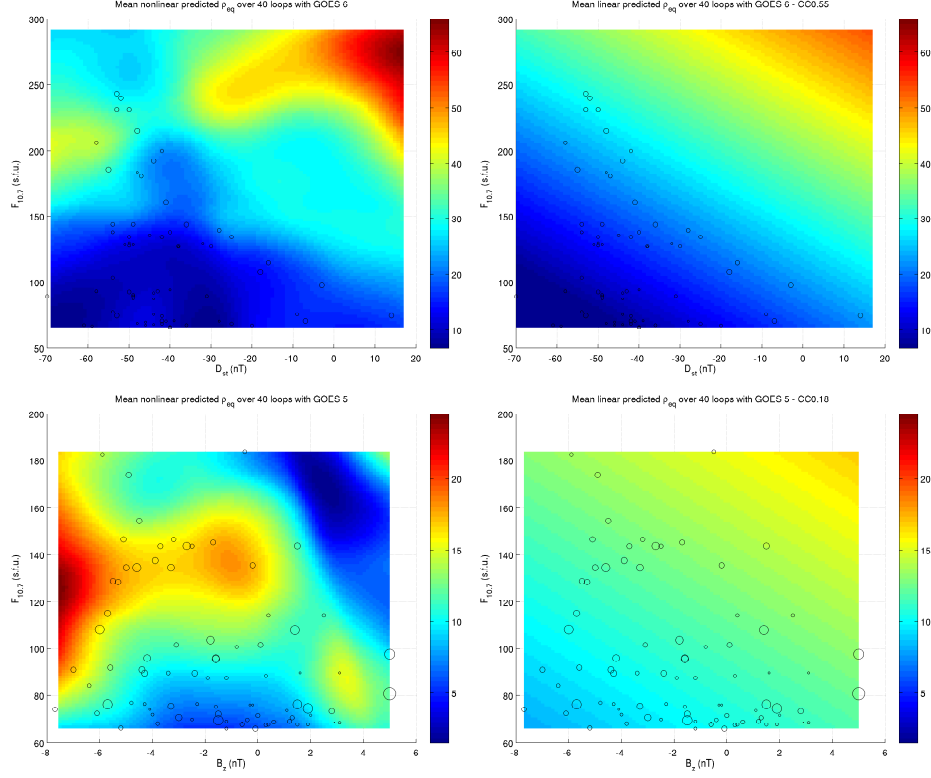


Figure 2.3: Nonlinear models (left) vs linear models (right) of  $\rho_{eq}$

### 2.2.5 Comparison to Linear Model

Nonlinear models differ from linear models by incorporating some method for accounting for effects within a domain that are not seen across the entire domain. Though both models can be given the same inputs, and trained on the same outputs, the models themselves can fundamentally differ. Linear models are also generally simple to interpret (e.g.  $y = 2 * x$  means for every change in  $x$ ,  $y$  changes by double that amount.) Nonlinear models, on the other hand, often have no simple interpretation and must be approached by testing for a range of parameters in the model to map out resulting outputs and make some interpretation of the underlying structure.

Nonlinear models can be compared to a linear model of the same data in order to assess the usefulness of accounting for nonlinear features. If both models result in similar correlation values, it can be said that the nonlinear model offers no extra insight into the

structure of the system and the relationships therein.

### **2.2.6 Summary**

Nonlinear models are a useful addition to linear models by allowing for better approximations to more complex physical systems, where the entire system may not fit a linear model or may have localized dependencies.

## Chapter 3: Measurements

The measurements can, to a certain extent, be broken into three main components: those pertaining to the solar wind, those from the magnetosphere in general, and those specific to the plasmasphere. An example of all the combined data sources is shown in Figure 3.1, providing solar wind variables  $B_z$  and  $V_{SW}$ , solar variable  $F_{10.7}$ , plasmatrough variable  $\rho_{eq}$ , and magnetosphere/plasmasphere variable  $D_{st}$ .

Similarly, Figure 1.4 earlier showed the same variables before, during, and after the March 1989 geomagnetic storm as seen by GOES 6. This makes it clearer how the variables are interrelated, notably how short-timescale effects such as drops in  $B_z$  and  $D_{st}$  are connected, or longer time scale changes on  $F_{10.7}$  and  $V_{SW}$  are related. It also shows how the sparse availability of  $\rho_{eq}$  created challenges for this study, as discussed later.

### 3.1 Solar Wind

The solar wind is the largest driver of particle density in the magnetosphere **cite Temerin and Li [2002]? They say solar wind drives Dst, and Dst is coupled to magnetospheric density via the ring current?**, and as such is an important input for a plasmatrough model. Conditions such as magnetic field orientation and particle velocity are important considerations for whether the plasmasphere is expected to be compressed, saturated, or experiencing high variability. By adding these to a model that includes time delayed inputs, their effects can be accounted for and aid in categorizing the state of the plasmatrough.

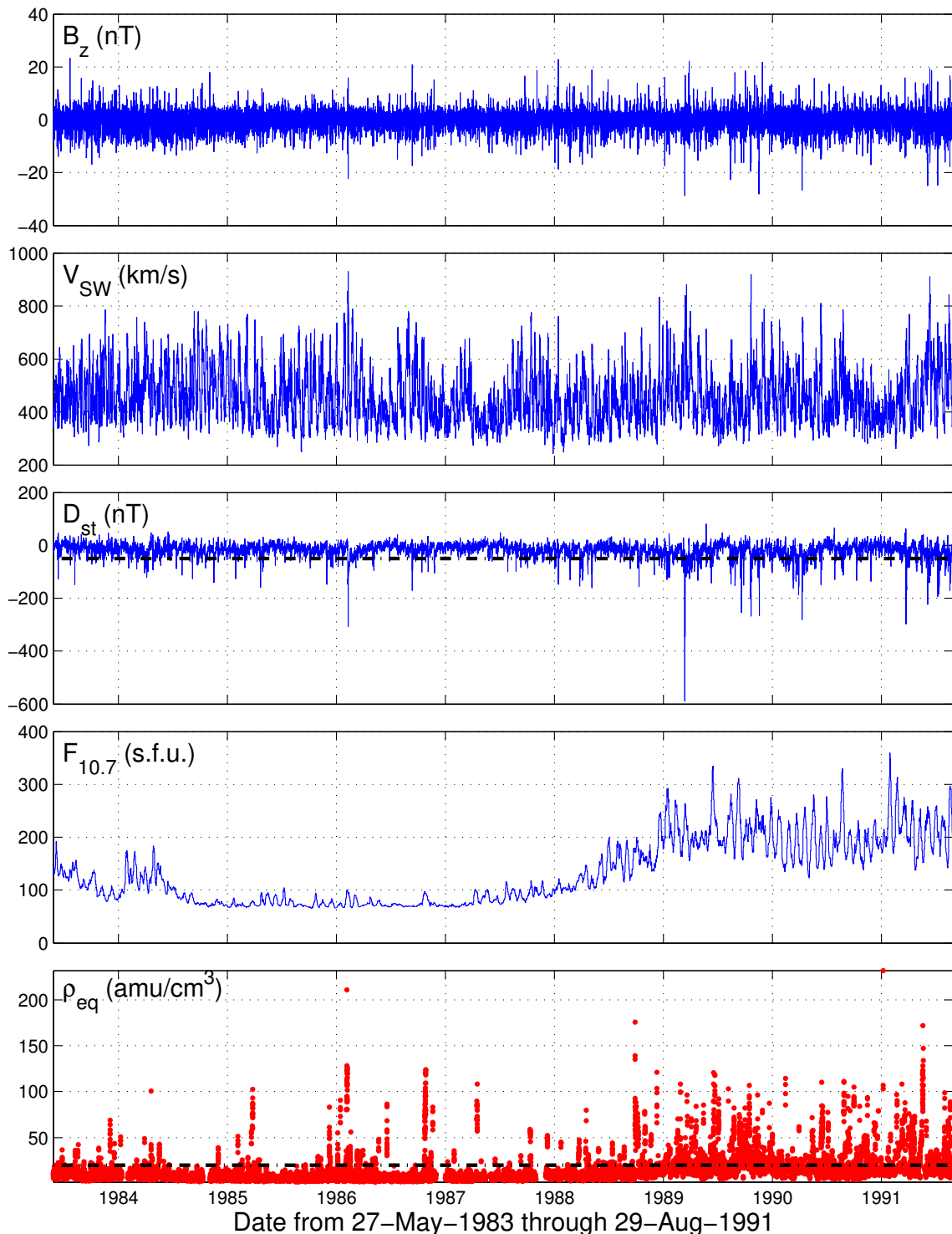


Figure 3.1: Data from GOES 6 with dashed lines indicating default storm thresholds

### 3.1.1 Source

Solar wind data for this dissertation is provided by the OMNIWeb service [King and Papiashvili, 2005], a combination of many satellites' data to create a uniform, high resolution, near-Earth set of solar wind measurements. The one-hour resolution dataset was used since the study is concerned with effects on timescales of longer than an hour, and to more easily compare to the other data sources used.

However, since the OMNIWeb data has gaps for some of the variables, Kondrashov et al. [2014] was used as they reliably reconstruct gaps to make a continuous, uniform data set. They used Singular Spectrum Analysis with synthetic gaps created by shifting real gaps from 1984-1995 data onto 1996-2007 data so that verification data would exist to test the effectiveness of their model.

### 3.1.2 Coverage

Low resolution (1-hour cadence) OMNI data is available from 1963 to present, but only the years of 1983-1992 were considered as they overlapped with the other data sets of interest. The data covers, but is not limited to: magnetic field strength in all three dimensions; solar wind proton density and temperature; the  $K_p$ ,  $AE$ ,  $F_{10.7}$ , and  $D_{st}$  indices; and varying levels of proton flux.

### 3.1.3 Data preparation

The only data cleaning required on the OMNI dataset was to convert fill values of 999.9 and 9999 to NaN, to be appropriate for use in data analysis. Of the variables included (see Coverage),  $B$ ,  $B_z$  (GSE and GSM), and Solar wind proton density and plasma speed all were missing about 35% of their data. The  $AE$  index was missing about 7% of its data, and all other variables were provided complete.

## 3.2 Geomagnetic

Geomagnetic data cover everything inside the magnetopause, but in this study will tend to refer specifically to information in the magnetosphere but not in the plasmasphere or ionosphere.

### 3.2.1 Source

The data come from Takahashi et al. [2010], which takes data from the Geostationary Operational Environmental Satellites (GOES) and uses a set of magnetic field models to relate Alfvén waves to equatorial mass density ( $\rho_{eq}$ ). By taking magnetic field vectors and applying spectral analysis, they find a set of fundamental harmonic frequencies of toroidal waves. Through testing, they find a strong linear dependence of the 27-day average third toroidal frequency ( $f_{T3.27d}$ ) on the similarly averaged  $F_{10.7}$  index, of the form:  $f_{T3.27d}(mHz) = 37.5 - 0.0972F_{10.7.27d}(sfu)$ . From there, they also find a linear relationship to the averaged  $\rho_{eq}$  in the form  $\log(\rho_{eq.27d}) = 0.421 + 0.00390F_{10.7.27d}$ , effectively linking the derived toroidal frequency to  $\rho_{eq}$ .

### 3.2.2 Coverage

The GOES satellites used in this study cover the years from 1980 to the end of 1991, often with overlapping years between satellites. The satellites themselves held a geostationary orbit at around  $6.62 R_E$  and collected data on a roughly 3-second cadence [GOE], which was then transformed onto a 10-minute cadence. Their position means they're almost always measuring properties of the plasmatrough, the region devoid of dense plasma just outside the plasmasphere.

### 3.2.3 Data preparation

The data were prepared by replacing fill values of 9999 with NaN and then narrowing results to only one satellite at a time to ideally remove any effects of satellite position or calibration

from the results. These data still had many temporal gaps (roughly 22% of the 10-minute intervals between the first and last point of GOES 6 had any data, the reasons for which are covered by Takahashi et al. [2010] when discussing the  $f_{T3\_30m}$  detection rate), so they were scaled onto a uniform 10-minute grid leaving missing points as NaN, allowing for easier data analysis and comparison to other data sets. The detection rate as a function of magnetic latitude and magnetic local time is shown in Figure 3.2.

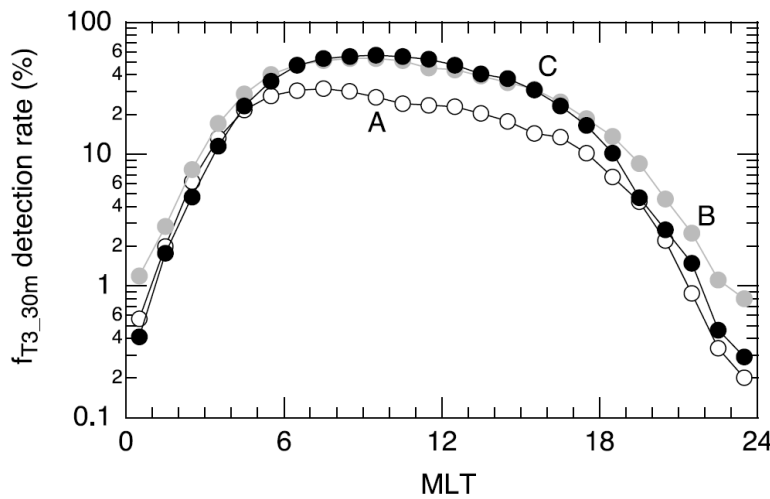


Figure 3.2: Detection rate of  $f_{T3\_30m}$  for magnetic latitudes of 5, 9, and 11 degrees (curves A, B, and C respectively). From [Takahashi et al., 2010].

In order to align the GOES data with the OMNI 1-hour cadence, the median of all existing values within 30 minutes on either side of each hour was taken. For hours with no existing values, a NaN was inserted to keep the cadence uniform. Two other methods were attempted: using the mean of each hour, centered on the hour, and using the median of the data on or within an hour after each time point (e.g. 7:00-7:59 would be combined into the 7:00 point). Both were found to have minimal effect on results.

### 3.3 Plasmasphere

Plasmasphere data covers the inner regions of the magnetosphere, bounded by the plasma-pause on the outer edge and the ionosphere on the inner edge. This puts it at a typical

distance of  $L = 3 - 5R_E$  [Carpenter and Anderson, 1992].

### 3.3.1 Source

Data for the plasmasphere also comes from the GOES and OMNI datasets previously discussed, but are often calculated as extensions of directly measured data either onboard the satellites or from ground stations, depending on the current extent of the plasmasphere and location of the satellite.

### 3.3.2 Coverage

Since the data come from the same sources as that of the magnetosphere, the coverage is largely the same with specifics covered in Takahashi et al. [2010], where any error associated with temporary conditions is overshadowed by the variance in effectiveness of the model itself.

### 3.3.3 Data preparation

The same preparation done for the magnetosphere applied to the plasmasphere data. Some specific analysis done in Takahashi et al. [2010] discusses how the spacecraft's geomagnetic location affected their ability to detect the necessary toroidal frequency, and thus estimate  $\rho_{eq}$ , so for some of the long-timescale averages, only certain MLTs were included. They also show that  $\rho_{eq}$  inversely correlates with geomagnetic activity (and, by extension, plasmapause location), so during long periods of no activity the plasmasphere extends beyond geosynchronous orbit, leading to measurements of  $\rho_{eq}$  reflecting density in the plasmasphere and not the plasmatrough.

**Include sources for CCMC model section?**

## Chapter 4: Analysis

### 4.1 Overview

While Figure 3.1 shows an overview of the most pertinent variables used in this study, some further analysis was done to determine any potential biases introduced by specifics of the satellite motion or derivations used. For example, Figure 4.1 shows that not only did data availability vary significantly with magnetic local time (MLT), a process that has been well established all the way back to whistler profiles of the plasmapause [Carpenter, 1966], but the values themselves vary significantly (e.g. AE models are better in the dawn sector and  $D_{st}$  models better at dusk [O'Brien and Moldwin, 2003].

### 4.2 Linear Correlations

This dependence was further investigated, and extended, by creating a simple linear model for each major variable in the database as well as combinations of some to investigate independent contributions to the total correlation (by testing how much correlation improved in a combined model over either of the constituent models.) The inputs were the median values of each variable for four hours before a  $D_{st}$  event onset, and they were trained to predict a median of the value at onset with the four hours following it. The models were trained on half of the dataset and tested on the other half for each satellite, and this was repeated with new random samples 100 times and then the median correlation values were taken. The results are shown in Table 4.1.

It can be seen that  $F_{10.7}$  almost always correlates the best with  $\rho_{eq}$ , but that there is significant variance between data from different satellites.

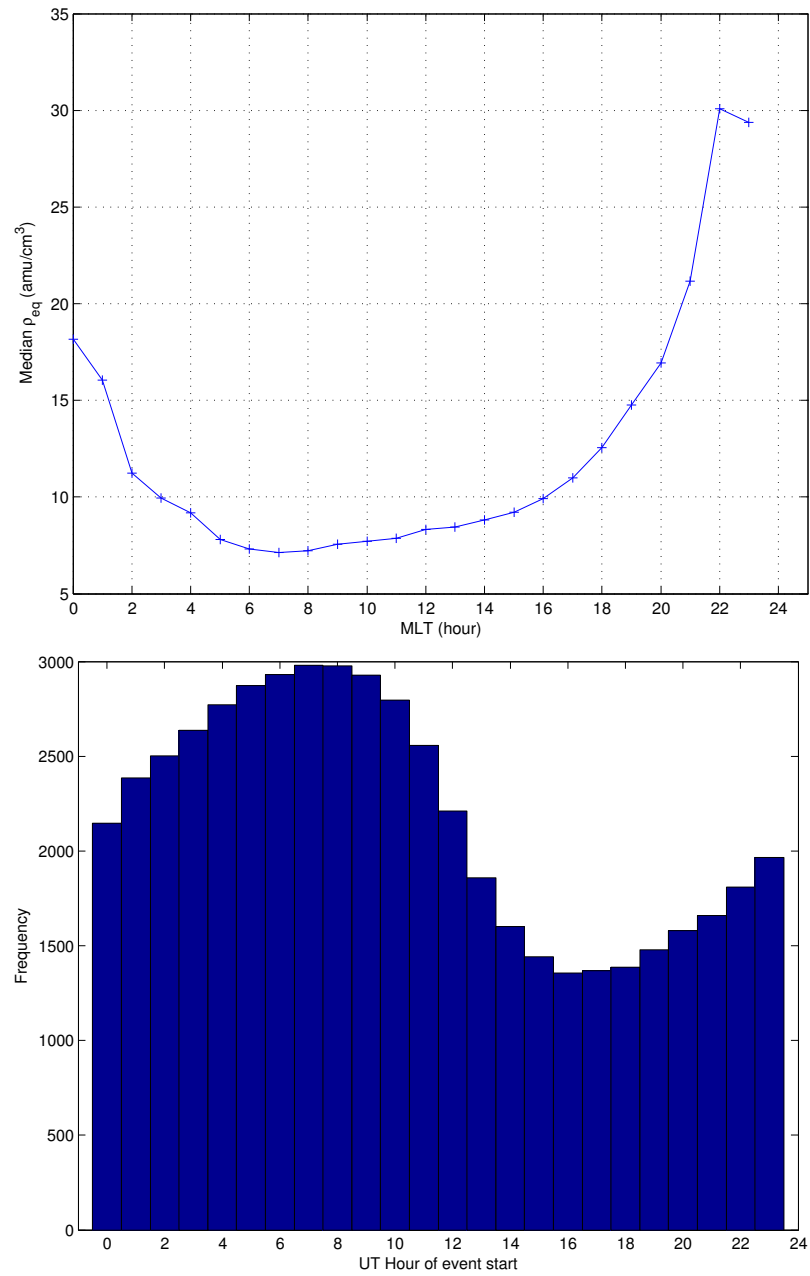


Figure 4.1: Median  $\rho_{eq}$  binned by local time, and availability of  $\rho_{eq}$  with local time.

	GOES 2	GOES 5	GOES 6	GOES 7
$DoY$	$-0.08 \pm 0.08$	$+0.14 \pm 0.13$	$-0.06 \pm 0.06$	$+0.09 \pm 0.10$
$MLT$	$-0.10 \pm 0.21$	$-0.07 \pm 0.12$	$+0.01 \pm 0.23$	$-0.06 \pm 0.05$
$B_z$	$+0.16 \pm 0.21$	$-0.13 \pm 0.15$	$+0.08 \pm 0.14$	$-0.07 \pm 0.06$
$V_{sw}$	$-0.04 \pm 0.10$	$+0.27 \pm 0.09$	$+0.06 \pm 0.11$	$-0.06 \pm 0.06$
$D_{st}$	$+0.26 \pm 0.17$	$+0.66 \pm 0.08$	$+0.06 \pm 0.13$	$+0.23 \pm 0.14$
$\rho_{sw}$	$+0.35 \pm 0.24$	$+0.63 \pm 0.31$	$+0.12 \pm 0.19$	$+0.36 \pm 0.17$
$F_{10.7}$	$+0.43 \pm 0.08$	$+0.12 \pm 0.12$	$+0.51 \pm 0.06$	$+0.40 \pm 0.06$
$B_z + V_{sw}$	$+0.11 \pm 0.17$	$+0.20 \pm 0.17$	$+0.12 \pm 0.10$	$-0.12 \pm 0.06$
$D_{st} + F_{10.7}$	$+0.44 \pm 0.09$	$+0.71 \pm 0.08$	$+0.54 \pm 0.07$	$+0.47 \pm 0.06$
<i>All</i>	$-0.03 \pm 0.19$	$+0.34 \pm 0.27$	$+0.61 \pm 0.11$	$+0.40 \pm 0.12$

Table 4.1: Table of linear model correlations showing the median of 100 random samples. Each sample trained on half of the data (via randomly selected rows of the least squares matrix) and tested on the other half

$Tr - T$	GOES 2	GOES 5	GOES 6	GOES 7
$DoY$	$+0.16 \pm 0.11$	$+0.02 \pm 0.16$	$+0.12 \pm 0.08$	$-0.01 \pm 0.12$
$MLT$	$+0.26 \pm 0.25$	$+0.16 \pm 0.14$	$+0.16 \pm 0.26$	$+0.11 \pm 0.07$
$B_z$	$+0.06 \pm 0.24$	$+0.27 \pm 0.18$	$+0.05 \pm 0.17$	$+0.14 \pm 0.08$
$V_{sw}$	$+0.11 \pm 0.13$	$+0.02 \pm 0.13$	$+0.03 \pm 0.13$	$+0.12 \pm 0.08$
$D_{st}$	$+0.02 \pm 0.21$	$+0.01 \pm 0.12$	$+0.06 \pm 0.16$	$+0.00 \pm 0.17$
$\rho_{sw}$	$+0.01 \pm 0.29$	$+0.01 \pm 0.37$	$+0.04 \pm 0.22$	$-0.03 \pm 0.21$
$F_{10.7}$	$-0.01 \pm 0.11$	$+0.04 \pm 0.16$	$+0.00 \pm 0.08$	$+0.03 \pm 0.08$
$B_z + V_{sw}$	$+0.15 \pm 0.20$	$+0.17 \pm 0.20$	$+0.08 \pm 0.12$	$+0.24 \pm 0.08$
$D_{st} + F_{10.7}$	$+0.05 \pm 0.12$	$-0.02 \pm 0.11$	$+0.01 \pm 0.10$	$+0.03 \pm 0.08$
<i>All</i>	$+0.64 \pm 0.22$	$+0.54 \pm 0.28$	$+0.16 \pm 0.14$	$+0.25 \pm 0.13$

Table 4.2: Table of differences in linear training-testing models, where each correlation is the median correlation of 100 random samples. Each sample trained on half of the data (via randomly selected rows of the least squares matrix) and tested on the other half

### 4.3 Nonlinear Correlations

Similarly for a neural net model with the same input and target structure as the linear model, but training on a randomly selected 70% of the data, testing on another 15%, and validating on the remaining 15%, Table 4.3 shows the resulting correlation values for the validation data set.

It should be noted that nonlinear modeling is much more susceptible to overfitting than linear modeling [cite?](#) due to the higher order of fitting done on training and validation data, as well as the lack of a straight-forward optimal error-minimization method such as least squares regression. This is why some models, such as that including every possible variable, correlate worse than models of just a few parts. Where a linear model can minimize error by

	GOES 2	GOES 5	GOES 6	GOES 7
<i>DoY</i>	+0.05 ± 0.31	+0.31 ± 0.30	+0.32 ± 0.22	+0.12 ± 0.17
<i>MLT</i>	+0.29 ± 0.41	+0.15 ± 0.34	+0.40 ± 0.32	+0.17 ± 0.21
$B_z$	+0.24 ± 0.23	+0.21 ± 0.28	+0.17 ± 0.19	-0.00 ± 0.20
$V_{sw}$	+0.20 ± 0.25	+0.36 ± 0.19	+0.19 ± 0.24	+0.06 ± 0.18
$D_{st}$	+0.08 ± 0.27	+0.18 ± 0.25	+0.02 ± 0.17	+0.18 ± 0.24
$\rho_{sw}$	+0.02 ± 0.29	+0.25 ± 0.42	+0.20 ± 0.22	+0.12 ± 0.29
$F_{10.7}$	+0.26 ± 0.27	+0.32 ± 0.29	+0.48 ± 0.25	+0.36 ± 0.15
$B_z + V_{sw}$	+0.11 ± 0.25	+0.20 ± 0.38	+0.15 ± 0.21	+0.02 ± 0.17
$D_{st} + F_{10.7}$	+0.17 ± 0.25	+0.21 ± 0.32	+0.47 ± 0.15	+0.35 ± 0.17
<i>All</i>	+0.21 ± 0.41	+0.67 ± 0.40	+0.60 ± 0.35	+0.17 ± 0.33

Table 4.3: Table of nonlinear model test correlations showing the median of 100 random samples. Each sample trained on half of the data (via randomly selected rows of the least squares matrix) and tested on the other half

$Tr - T$	GOES 2	GOES 5	GOES 6	GOES 7
<i>DoY</i>	+0.48 ± 0.36	+0.17 ± 0.33	+0.18 ± 0.24	+0.27 ± 0.23
<i>MLT</i>	+0.31 ± 0.40	+0.28 ± 0.42	+0.31 ± 0.36	+0.28 ± 0.26
$B_z$	+0.14 ± 0.27	+0.29 ± 0.33	+0.20 ± 0.27	+0.20 ± 0.19
$V_{sw}$	+0.27 ± 0.31	+0.22 ± 0.31	+0.20 ± 0.27	+0.24 ± 0.19
$D_{st}$	+0.37 ± 0.32	+0.27 ± 0.32	+0.18 ± 0.21	+0.21 ± 0.24
$\rho_{sw}$	+0.31 ± 0.30	+0.16 ± 0.42	+0.24 ± 0.27	+0.47 ± 0.37
$F_{10.7}$	+0.19 ± 0.28	+0.19 ± 0.29	+0.15 ± 0.25	+0.18 ± 0.26
$B_z + V_{sw}$	+0.28 ± 0.31	+0.26 ± 0.32	+0.28 ± 0.22	+0.23 ± 0.19
$D_{st} + F_{10.7}$	+0.30 ± 0.29	+0.20 ± 0.32	+0.14 ± 0.19	+0.20 ± 0.16
<i>All</i>	+0.51 ± 0.58	+0.47 ± 0.60	+0.41 ± 0.36	+0.46 ± 0.43

Table 4.4: Table of differences in nonlinear training-testing models, where each correlation is the median correlation of 100 random samples. Each sample trained on half of the data (via randomly selected rows of the least squares matrix) and tested on the other half

zeroing out variables without useful information, the neural net will try to incorporate the information anyway and end up overfitting. Table 4.4 shows how significant the differences are between training data and testing data by subtracting the median correlations from both data sets from each other, and doing the root mean squared (RMS) error as the combination of the two constituent errors.

#### 4.4 $F_{10.7}$ Dependence

Takahashi et al. [2010] showed a strong correlation between the 27-day averaged  $F_{10.7}$  index of solar activity and the averaged equatorial mass density ( $\rho_{eq}$ ). This was chosen as a starting place for verifying the data analysis routines developed for this dataset, so as

to show that data input, averaging, and interpolation were all done in a reasonable and reproducible manner. Figure 4.2.a shows the strong correlation seen previously, and reasonably reproduces Figure 13.b from Takahashi et al. [2010] for the years covered by GOES 6. Figure 4.3 shows the effects of long-time-scale averaging on the overall correlation of the two variables, suggesting that the connection is more influential long-term.

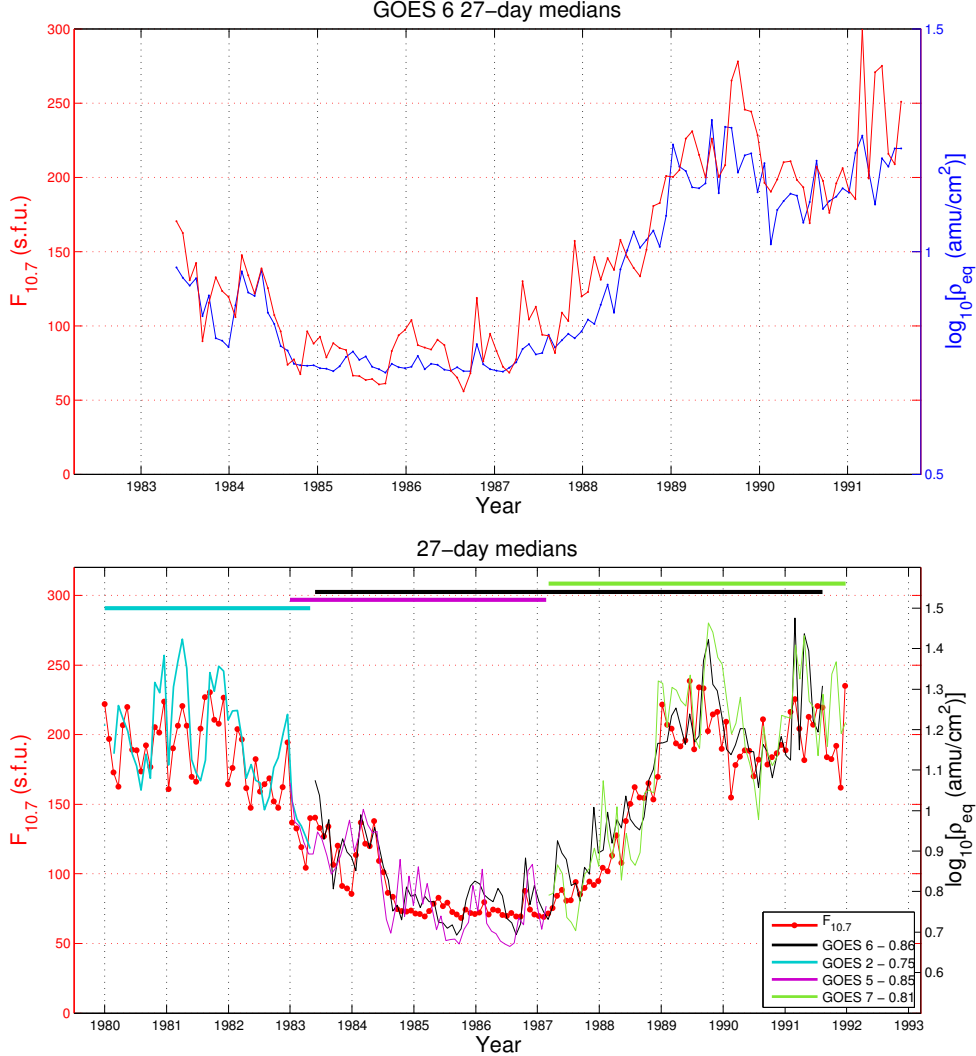


Figure 4.2: Top: Comparing  $F_{10.7,27d}$  and  $\log(\rho_{eq,27d})$  using GOES 6 data. Bottom: Same as top, but all available satellites

The dependence was then analyzed in a more nonlinear manner by investigating the behavior of storms under different  $F_{10.7}$  conditions. The hypothesis being that solar activity

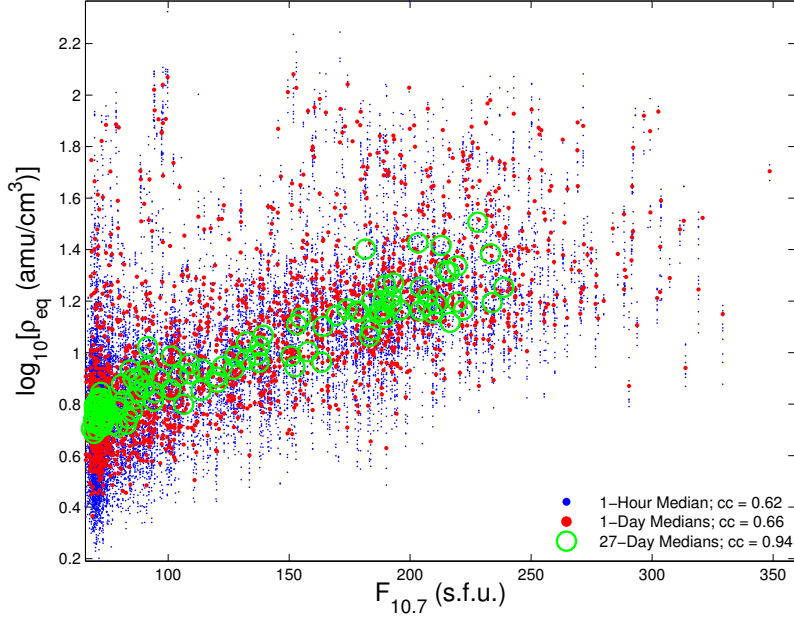


Figure 4.3:  $F_{10.7}$  and  $\log(\rho_{eq})$  correlation at varying time scales

would drive both geomagnetic storms and, consequently,  $\rho_{eq}$ . By separating storms into bins based on the median value of  $F_{10.7}$ , then breaking those two bins into another two bins each separated by their respective medians, a profile of all storm behavior based on  $F_{10.7}$  is obtained. Figure 4.4 shows the results of this across the events where  $D_{st}$  crossed below the  $-50$  nT threshold.

Figure 4.4.a shows that  $\rho_{eq}$  reacts to decreases in  $D_{st}$ , but seemingly only during periods of higher solar activity. Since higher  $F_{10.7}$  also correlates with a higher baseline  $\rho_{eq}$ , this effect could be due to saturation of the plasmasphere from the increased solar activity. It should also be noted that this trend isn't seen as strongly for all satellites. GOES 2 and 6 show a significant spike and baseline shift, while GOES 7 and 5 lack the significant spike and shift respectively.

Figure 4.4.b shows that though all events are selected based on a  $D_{st}$  threshold, the behavior before and after the storm is affected by  $F_{10.7}$ . For low solar activity events, the  $D_{st}$  changes are more sudden and severe, coming from and going back to a more positive baseline. High solar activity events have a longer recovery period.

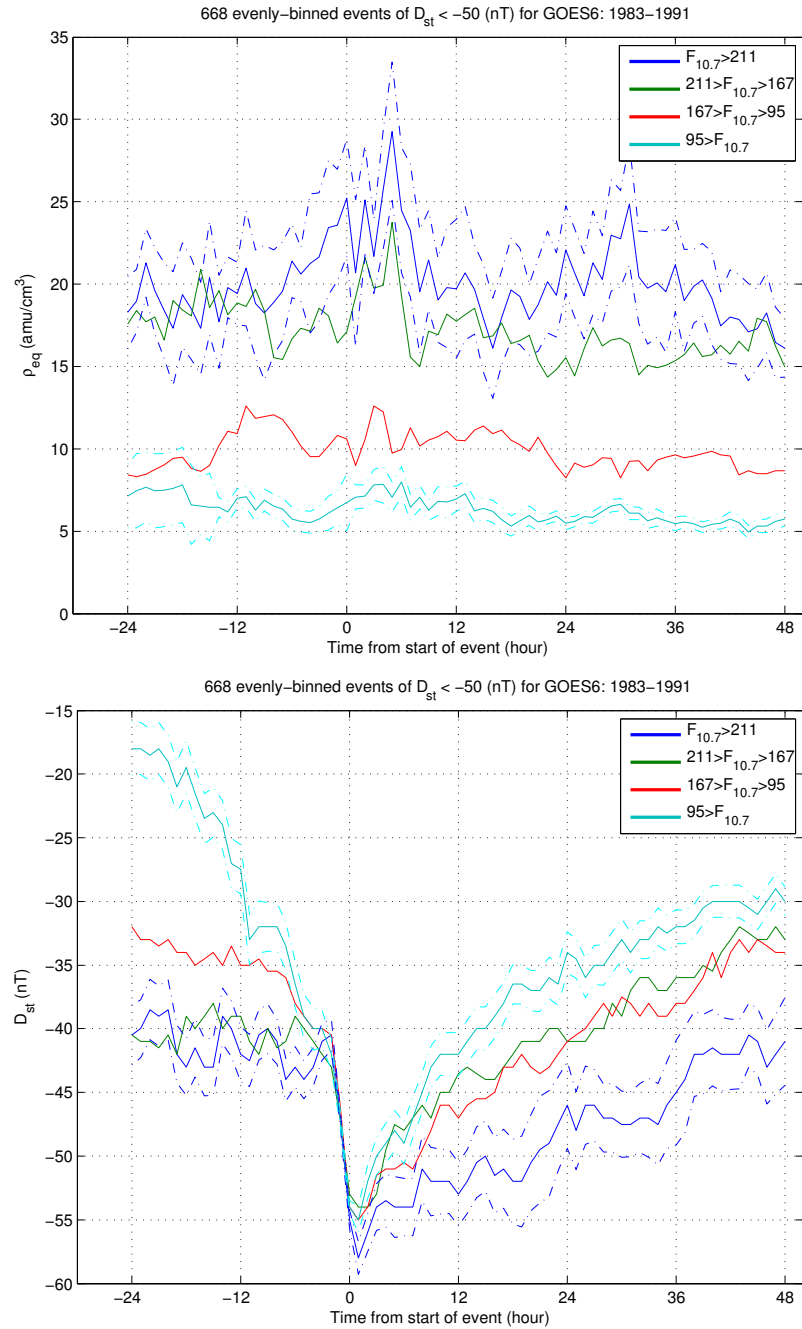


Figure 4.4:  $\rho_{eq}$  and  $D_{st}$  of events binned by median  $F_{10.7}$  values. **Temerin and Li  $D_{st}$  model. Bz seems to have little impact.**

## 4.5 $B_z$ Dependence

Similar to the  $F_{10.7}$  dependence, tests were done to see if event behavior varied with the  $z$ -component of the interplanetary magnetic field (IMF). It's well established that the orientation of  $B_z$  has a strong correlation with the strength of geomagnetic storms [Takahashi et al., 2010], so events were found based on a threshold of  $\rho_{eq} \geq 20 \text{ amu/cm}^3$ . These events were then binned by both the median  $B_z$  at and four hours after threshold crossing, and  $B_z$  at and four hours before threshold crossing. Figure 4.5 shows both cases.

For each binning method, a two sample t-test was performed for each hour to determine if the samples in each bin had significantly different means from those of the other bin. As there are 73 hours to perform a t-test on, a 95% confidence interval could be expected to have at least four randomly significant results. Because of this, the one significant t-test result for events binned by pre-onset  $B_z$  can not confirm that such a division shows significantly different behaviors, whereas the 14 significant test results for post-onset  $B_z$  can be said to show a significant division in behavior between the bins. This physically suggests that the further into a  $\rho_{eq}$  increase you get, the more  $B_z$  orientation impacts the long-term recovery to normal conditions (and indeed moving the window further in time did continue to show significance, but weakly and with no obvious trend). If instead of splitting into equal-number bins, the division is based on positive or negative  $B_z$ , either time window produces seven or more significant results, but with the added complication that one bin has twice as many samples as the other and may be biased by averaging or the lack thereof.

Temerin and Li [2002] discuss the impact of  $B_z$  on their model of  $D_{st}$  showing a seasonal variation of  $D_{st}$ . Figure 4.6 shows how  $D_{st}$  seems to vary with day of year (DoY) in our nonlinear models. These plots show a nonlinear model trained on all data, then predicted over a uniform grid of points to visualize the underlying structure of the model. The top panel predicts  $D_{st}$  using DoY as an input, showing the average model output over 40 ensemble models, along with the standard deviation at each point. The bottom panel predicts  $D_{st}$  using both DoY and  $B_z$  as inputs, also using a 40-member ensemble average,

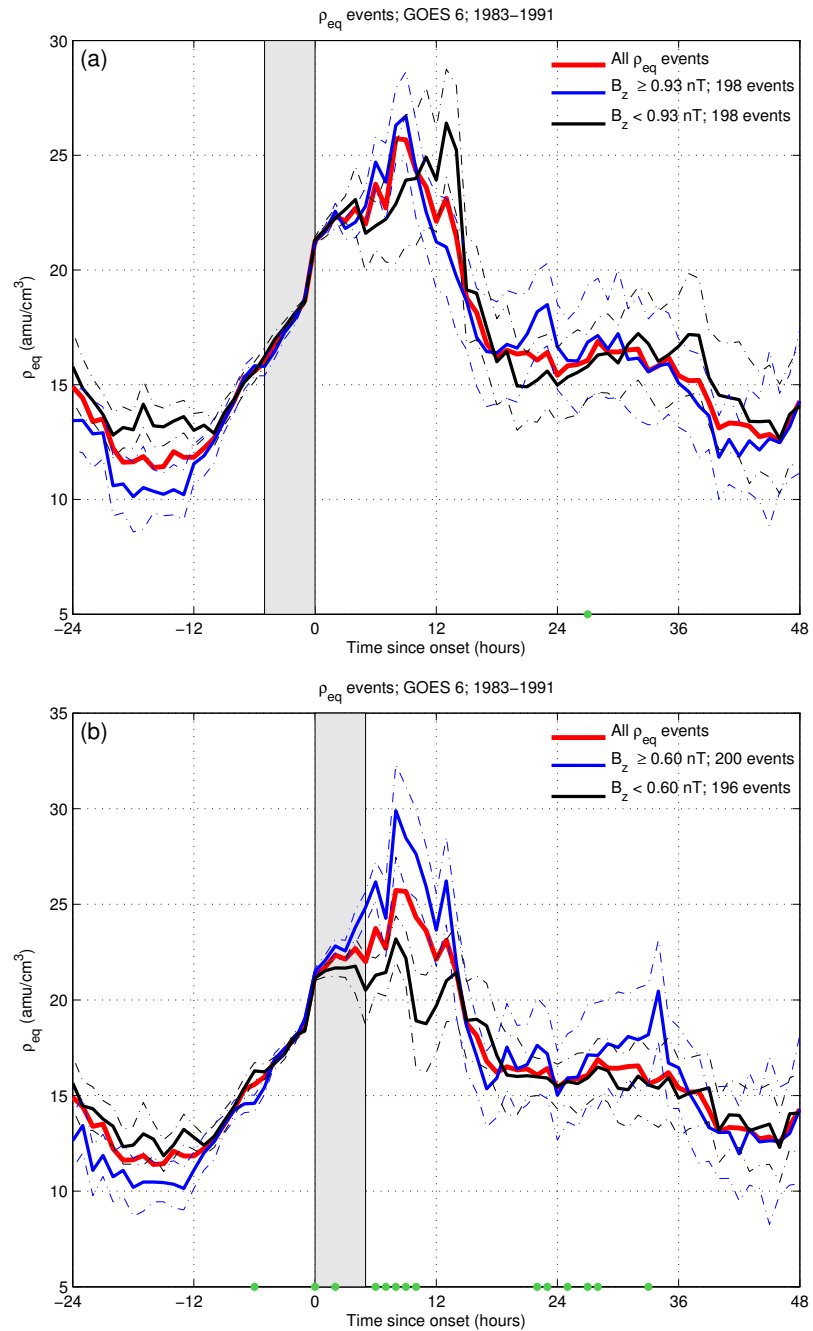


Figure 4.5:  $\rho_{eq}$  events binned by median  $B_z$  before and after event onset

but with the actual datapoints overlaid to give an idea of what the structure may be derived from. Marker size in this panel is based on the value of  $D_{st}$  at that point. It seems to support the idea of a seasonal variation, and weakly the idea that  $B_z$  also plays a part in that relationship.

**Moldwin 2014 long duration southward IMF Bz 10.1002/2013JA018937**

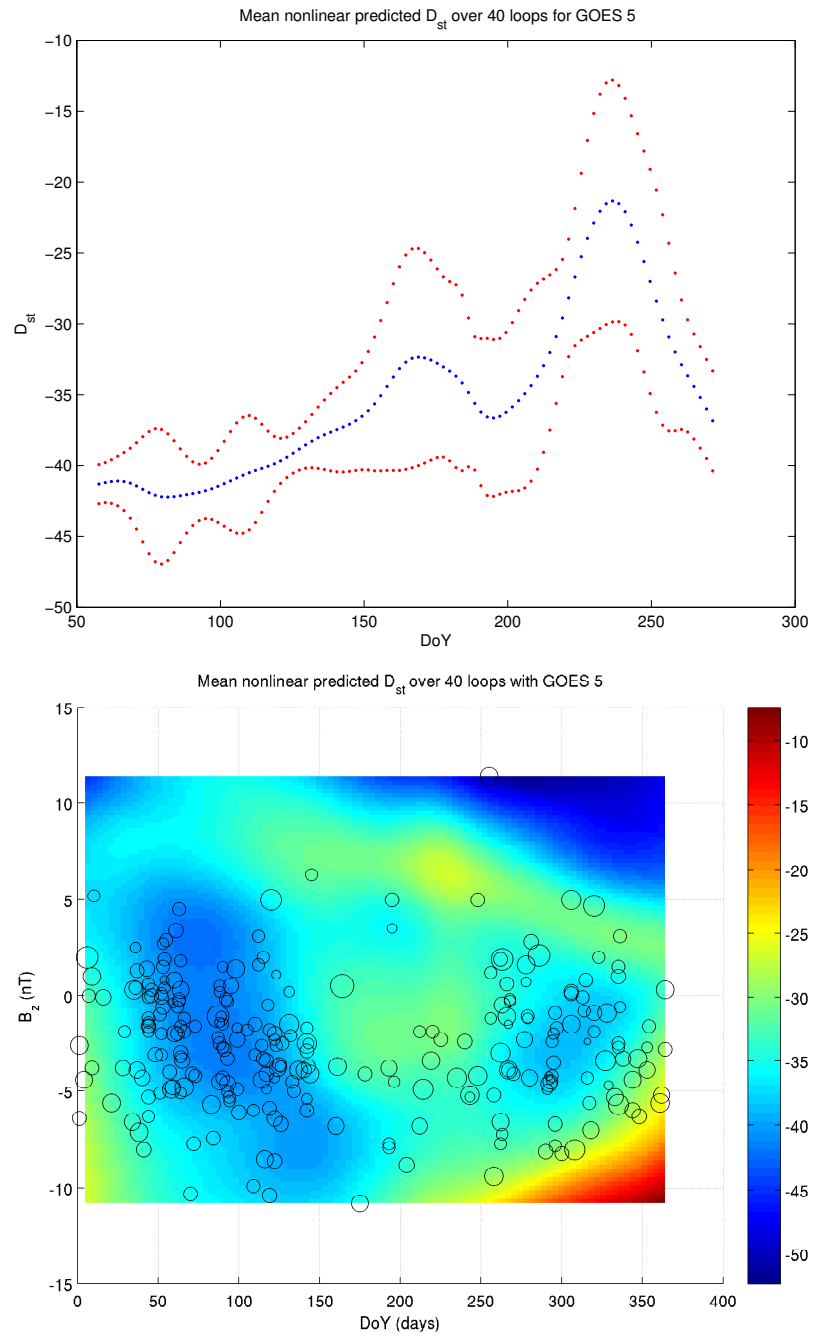


Figure 4.6:  $D_{st}$  predicted by nonlinear model of day of year. Bottom: Same, but including a dimension for  $B_z$ . **See/improve DoYDst figure**

## Chapter 5: Onset Classification

### 5.1 Method

Since forecasting actual values for  $\rho_{eq}$  isn't always viable or accurate, an attempt was made to model  $\rho_{eq}$  event onsets as a classification problem whereby an onset timestep (the one in which the  $20 \text{ amu/cm}^3$  threshold was crossed) was defined as a “1”, and any other time defined as a “0”. By then passing in relevant measurements such as KP,  $F_{10.7}$ , and  $V_{SW}$ , a predictive classification could be made based on these conditions.

Two formats and two time scales were tested: one format consisting of passing in an entire timeseries, where each prediction was based on the current and previous three timesteps as one set of inputs. The other format only considered time periods at and three hours before onset, but treated each time step as its own input and classification. The two time scales were hourly and daily medians of values.

### 5.2 Results

Figure 5.1 shows that trying to predict events on an hourly timescale using only the onset hour and three hours before leads to a model that predicts no onsets. Using daily values, however, results in a model where almost a third of the onsets are correctly detected, but only half of the predicted onsets were actually onsets.

Using the full data set where each prediction was based on the current and previous three hours of inputs returned two models (daily and hourly) both of which predicted no onsets for  $\rho_{eq}$  events.

In an attempt to find out what conditions best lead to a correct prediction, histograms were made of the conditions associated with a correctly predicted onset vs those of an

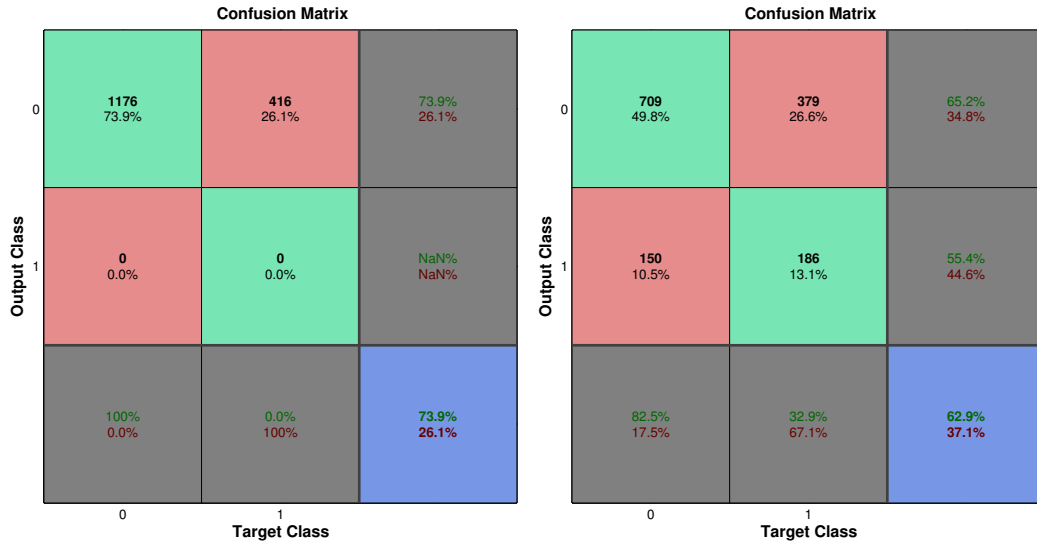


Figure 5.1: Prediction confusion matrix for hourly (left) and daily (right)  $\rho_{eq}$  onset events

unpredicted onset. Figure 5.2 shows this for the three **Updated if more added** variables used.

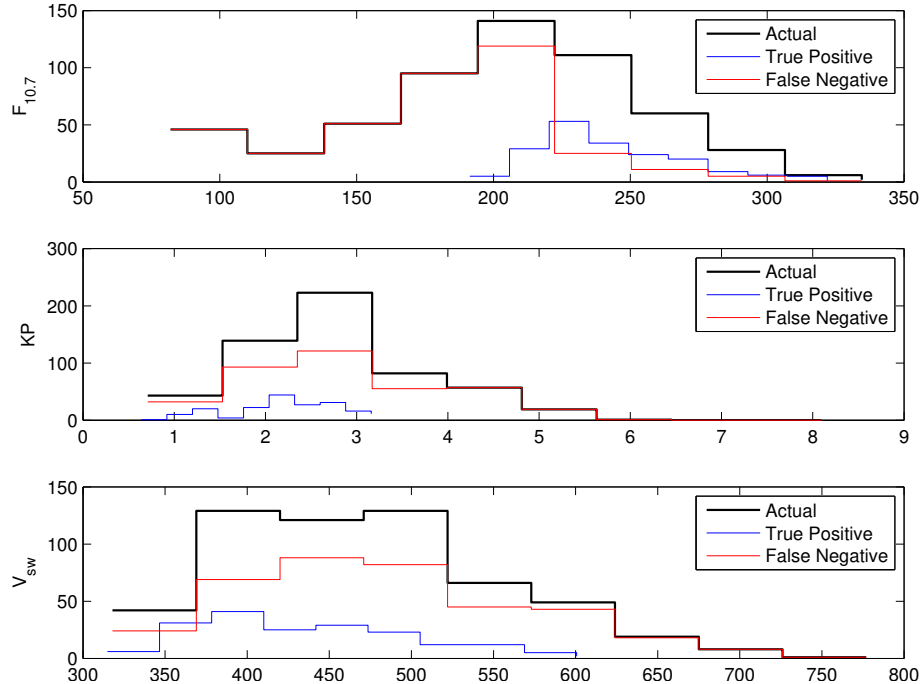


Figure 5.2: Histogram of onset conditions for  $\rho_{eq}$  events binned by correctness of prediction

It shows that the model tended to correctly predict onset more often when given a larger

value of  $F_{10.7}$ , but that all other variables seemed to have a similar distribution between their correct and incorrect predictions.

## **Appendix A: An Appendix**

This is an appendix. Here is a numbered appendix equation:

$$a^2 + b^2 = c^2. \quad (\text{A.1})$$

## Bibliography

- Access to GOES SEM data. URL <https://www.ngdc.noaa.gov/stp/satellite/goes/dataaccess.html>.
- J. Allen, L. Frank, H. Sauer, and P. Reiff. Effects of the March 1989 solar activity. *EOS Transactions*, 70:1479, November 1989. doi: 10.1029/89EO00409.
- R. Bala and P. Reiff. Improvements in short-term forecasting of geomagnetic activity. *Space Weather*, 10:S06001, June 2012. doi: 10.1029/2012SW000779.
- L. F. Bargatze, D. N. Baker, E. W. Hones, Jr., and R. L. McPherron. Magnetospheric impulse response for many levels of geomagnetic activity. *Journal of Geophysical Research*, 90:6387–6394, July 1985. doi: 10.1029/JA090iA07p06387.
- G. Brier and R. Allen. Verification of Weather Forecasts. *Compendium of Meteorology*, pages 841–848, 1951. URL <http://archive.org/stream/compendiumofmete00amer#page/840/mode/2up>.
- D. L. Carpenter. Whistler studies of the plasmapause in the magnetosphere: 1. Temporal variations in the position of the knee and some evidence on plasma motions near the knee. *J. Geophys. Res.*, 71:693–709, February 1966. doi: 10.1029/JZ071i003p00693.
- D. L. Carpenter and R. R. Anderson. An ISEE/Whistler model of equatorial electron density in the magnetosphere. *J. Geophys. Res.*, 97:1097–1108, February 1992. doi: 10.1029/91JA01548.
- D. L. Carpenter and J. Lemaire. Erosion and Recovery of the Plasmasphere in the

- Plasmapause Region. *Space Science Reviews*, 80:153–179, April 1997. doi: 10.1023/A:1004981919827.
- C. Carreau. Earth’s plasmasphere and the Van Allen belts, September 2013. URL <http://sci.esa.int/cluster/52831-earth-plasmasphere-and-the-van-allen-belts/>.
- R. C. Carrington. Description of a Singular Appearance seen in the Sun on September 1, 1859. *Monthly Notices of the Royal Astronomical Society*, 20:13–15, November 1859.
- CCMC. Community coordinated modeling center. URL <http://ccmc.gsfc.nasa.gov/>.
- S. Chapman and V. C. A. Ferraro. A new theory of magnetic storms. *Terrestrial Magnetism and Atmospheric Electricity (Journal of Geophysical Research)*, 36:77, 1931. doi: 10.1029/TE036i002p00077.
- C. R. Clauer, R. L. McPherron, C. Searls, and M. G. Kivelson. Solar wind control of auroral zone geomagnetic activity. *Geophysical Research Letters*, 8:915–918, August 1981. doi: 10.1029/GL008i008p00915.
- F. Darrouzet, V. Pierrard, S. Benck, G. Lointier, J. Cabrera, K. Borremans, N. Y. Ganushkina, and J. D. Keyser. Links between the plasmapause and the radiation belt boundaries as observed by the instruments CIS, RAPID, and WHISPER onboard Cluster. *Journal of Geophysical Research (Space Physics)*, 118:4176–4188, July 2013. doi: 10.1002/jgra.50239.
- T. N. Davis and M. Sugiura. Auroral electrojet activity index AE and its universal time variations. *J. Geophys. Res.*, 71:785–801, February 1966. doi: 10.1029/JZ071i003p00785.
- R. C. Elphic, L. A. Weiss, M. F. Thomsen, D. J. McComas, and M. B. Moldwin. Evolution of plasmaspheric ions at geosynchronous orbit during times of high geomagnetic activity. *Geophysical Research Letters*, 23:2189–2192, 1996. doi: 10.1029/96GL02085.
- S. F. Fung, X. Shao, and L. C. Tan. Long-term variations of the electron slot region and

global radiation belt structure. *Geophys. Res. Lett.*, 33:L04105, February 2006. doi: 10.1029/2005GL024891.

D. L. Gallagher, P. D. Craven, R. H. Comfort, and T. E. Moore. On the azimuthal variation of core plasma in the equatorial magnetosphere. *J. Geophys. Res.*, 100:23597–23606, December 1995. doi: 10.1029/95JA02100.

D. L. Gallagher, P. D. Craven, and R. H. Comfort. Global core plasma model. *J. Geophys. Res.*, 105:18, August 2000. doi: 10.1029/1999JA000241.

M. Ghil, P. Yiou, S. Hallegatte, B. D. Malamud, P. Naveau, A. Soloviev, P. Friederichs, V. Keilis-Borok, D. Kondrashov, V. Kossobokov, O. Mestre, C. Nicolis, H. W. Rust, P. Shebalin, M. Vrac, A. Witt, and I. Zaliapin. Extreme events: dynamics, statistics and prediction. *Nonlinear Processes in Geophysics*, 18:295–350, May 2011. doi: 10.5194/npg-18-295-2011.

T. Gold. Origin of the Radiation Near the Earth Discovered by Means of Satellites. *Nature*, 183:355–358, February 1959. doi: 10.1038/183355a0.

W. D. Gonzalez, J. A. Joselyn, Y. Kamide, H. W. Kroehl, G. Rostoker, B. T. Tsurutani, and V. M. Vasyliunas. What is a geomagnetic storm? *J. Geophys. Res.*, 99:5771–5792, April 1994. doi: 10.1029/93JA02867.

J. T. Gosling, D. J. McComas, J. L. Phillips, and S. J. Bame. Geomagnetic activity associated with earth passage of interplanetary shock disturbances and coronal mass ejections. *Journal Of Geophysical Research*, 96:7831–7839, May 1991. doi: 10.1029/91JA00316.

P. Heidke. Berechnung des Erfolges und der Güte der Windstärkevorhersagen im Sturmwarnungsdienst. *Geografiska Annaler*, 8:310–349, 1926. URL <http://www.jstor.org/stable/519729?seq=4>.

- J. V. Hernandez, T. Tajima, and W. Horton. Neural net forecasting for geomagnetic activity. *Geophysical Research Letters*, 20:2707–2710, December 1993. doi: 10.1029/93GL02848.
- A. Keiling. Alfvén Waves and Their Roles in the Dynamics of the Earth’s Magnetotail: A Review. *Space Sci. Rev.*, 142:73–156, February 2009. doi: 10.1007/s11214-008-9463-8.
- J. H. King and N. E. Papitashvili. Solar wind spatial scales in and comparisons of hourly Wind and ACE plasma and magnetic field data. *Journal of Geophysical Research (Space Physics)*, 110:A02104, February 2005. doi: 10.1029/2004JA010649.
- A. J. Klimas, D. Vassiliadis, and D. N. Baker. Dst index prediction using data-derived analogues of the magnetospheric dynamics. *Journal of Geophysical Research*, 103:20435–20448, September 1998. doi: 10.1029/98JA01559.
- D. Kondrashov, R. Denton, Y. Y. Shprits, and H. J. Singer. Reconstruction of gaps in the past history of solar wind parameters. *Geophys. Res. Lett.*, 41:2702–2707, April 2014. doi: 10.1002/2014GL059741.
- J Lemaire. *The Earth’s Plasmasphere*. Cambridge University Press, Cambridge, U.K. New York, 1998. ISBN 9780521430913.
- T. M. Loto’aniu, C. L. Waters, B. J. Fraser, and J. C. Samson. Plasma mass density in the plasmatrough: Comparison using ULF waves and CRRES. *Geophys. Res. Lett.*, 26: 3277–3280, 1999. doi: 10.1029/1999GL003641.
- M. B. Moldwin, L. Downward, H. K. Rassoul, R. Amin, and R. R. Anderson. A new model of the location of the plasmapause: CRRES results. *Journal of Geophysical Research (Space Physics)*, 107:1339, November 2002. doi: 10.1029/2001JA009211.
- Homer Newell. *Beyond the Atmosphere Early Years of Space Science*. Dover Publications, City, 2011. ISBN 0486135659. URL <http://history.nasa.gov/SP-4211/contents.htm>.

T. P. O'Brien and M. B. Moldwin. Empirical plasmapause models from magnetic indices. *Geophys. Res. Lett.*, 30:1152, February 2003. doi: 10.1029/2002GL016007.

National Oceanic and Atmospheric Administration. NOAA Space Weather Scales, 2005. URL <http://www.swpc.noaa.gov/NOAAAscales/>.

R. S. Richardson. Sun-Spots and Magnetic Storms. *Leaflet of the Astronomical Society of the Pacific*, 2:133, 1936.

Willie Soon and Steven H. Yaskell. *The Maunder Minimum and the Variable Sun-earth Connection*. World Scientific, 2003. ISBN 9789812382757.

David P. Stern. The art of mapping the magnetosphere. *Journal of Geophysical Research: Space Physics*, 99(A9):17169–17198, 1994. ISSN 2156-2202. doi: 10.1029/94JA01239. URL <http://dx.doi.org/10.1029/94JA01239>.

K. Takahashi, R. E. Denton, R. R. Anderson, and W. J. Hughes. Mass density inferred from toroidal wave frequencies and its comparison to electron density. *Journal of Geophysical Research (Space Physics)*, 111:A01201, January 2006. doi: 10.1029/2005JA011286.

K. Takahashi, R. E. Denton, and H. J. Singer. Solar cycle variation of geosynchronous plasma mass density derived from the frequency of standing Alfvén waves. *Journal of Geophysical Research (Space Physics)*, 115:A07207, July 2010. doi: 10.1029/2009JA015243.

M. Temerin and X. Li. A new model for the prediction of Dst on the basis of the solar wind. *Journal of Geophysical Research (Space Physics)*, 107:1472, December 2002. doi: 10.1029/2001JA007532.

M. F. Thomsen. Why K<sub>p</sub> is such a good measure of magnetospheric convection. *Space Weather*, 2:S11004, November 2004. doi: 10.1002/2004SW000089.

N. A. Tsyganenko and M. I. Sitnov. Modeling the dynamics of the inner magnetosphere during strong geomagnetic storms. *Journal of Geophysical Research (Space Physics)*, 110: A03208, March 2005. doi: 10.1029/2004JA010798.

D. Vassiliadis, R. S. Weigel, D. N. Baker, S. G. Kanekal, and A. J. Klimas. Probing the solar wind-inner magnetospheric coupling: validation of relativistic electron flux models. *Journal of Atmospheric and Solar-Terrestrial Physics*, 66:1399–1409, October 2004. doi: 10.1016/j.jastp.2004.03.025.

Martin Walt. *Introduction to Geomagnetically Trapped Radiation*. Cambridge University Press, Cambridge New York, 1994. ISBN 9780521431439.

R. S. Weigel. Solar wind time history contribution to the day-of-year variation in geomagnetic activity. *Journal of Geophysical Research (Space Physics)*, 112:A10207, October 2007. doi: 10.1029/2007JA012324.

R. S. Weigel, T. Detman, E. J. Rigler, and D. N. Baker. Decision theory and the analysis of rare event space weather forecasts. *Space Weather*, 4:05002, May 2006. doi: 10.1029/2005SW000157.

Y. I. Yermolaev and M. Y. Yermolaev. Statistic study on the geomagnetic storm effectiveness of solar and interplanetary events. *Advances in Space Research*, 37:1175–1181, 2006. doi: 10.1016/j.asr.2005.03.130.

S. L. Young, R. E. Denton, B. J. Anderson, and M. K. Hudson. Magnetic field line curvature induced pitch angle diffusion in the inner magnetosphere. *Journal of Geophysical Research (Space Physics)*, 113:A03210, March 2008. doi: 10.1029/2006JA012133.

J. Zhang, M. W. Liemohn, J. U. Kozyra, M. F. Thomsen, H. A. Elliott, and J. M. Weygand. A statistical comparison of solar wind sources of moderate and intense geomagnetic storms at solar minimum and maximum. *Journal of Geophysical Research (Space Physics)*, 111: A01104, January 2006. doi: 10.1029/2005JA011065.

J. Zhang, I. G. Richardson, D. F. Webb, N. Gopalswamy, E. Huttunen, J. C. Kasper, N. V. Nitta, W. Poomvises, B. J. Thompson, C.-C. Wu, S. Yashiro, and A. N. Zhukov. Solar

and interplanetary sources of major geomagnetic storms ( $Dst \leq -100$  nT) during 1996-2005. *Journal of Geophysical Research (Space Physics)*, 112:A10102, October 2007. doi: 10.1029/2007JA012321.

## **Curriculum Vitae**

Include your *curriculum vitae* here detailing your background, education, and professional experience.